

Stress granules and mTOR are regulated by membrane atg8ylation during lysosomal damage

Jingyue Jia^{1,2}, Fulong Wang^{1,2}, Zambarlal Bhujabal³, Ryan Peters^{1,2}, Michal Mudd^{1,2}, Thabata Duque^{1,2}, Lee Allers^{1,2}, Ruheena Javed^{1,2}, Michelle Salemi⁴, Christian Behrends⁵, Brett Phinney⁴, Terje Johansen³, and Vojo Deretic^{1,2,6*}

¹Autophagy, Inflammation and Metabolism Center of Biochemical Research Excellence.

²Department of Molecular Genetics and Microbiology, University of New Mexico Health Sciences Center, 915 Camino de Salud, NE, Albuquerque, NM 87131, USA.

³Molecular Cancer Research Group, Institute of Medical Biology, The Arctic University of Norway, 9037 Tromsø, Norway

⁴Proteomics Core Facility, UC Davis Genome Center, University of California, Davis, CA 95616, USA.

⁵Munich Cluster of Systems Neurology, Ludwig-Maximilians-Universität München Feodor-Lynen Str. 17, 81377 München, Germany

⁶Lead Contact

*Correspondence:

Vojo Deretic, Ph.D.

Department of Molecular Genetics and Microbiology

University of New Mexico Health Sciences Center

915 Camino de Salud, NE

Albuquerque, NM 87131

U.S.A.

vderetic@salud.unm.edu

eTOC summary:

Lysosomal damage induces stress granule (SG) formation and translational reprogramming. The newly appreciated process of atg8ylation affects SG formation and concomitantly recruits SG core proteins NUFIP2 and G3BP1 to damaged lysosomes. These proteins independently of SG condensates and in coordination with galectin-8 inactivate mTOR via the Regulator-Rag complex.

Abstract

We report that lysosomal damage is a hitherto unknown inducer of stress granule (SG) formation and that the process termed membrane atg8ylation coordinates SG formation with mTOR inactivation during lysosomal stress. SGs were induced by lysosome-damaging agents including SARS-CoV-2^{ORF3a}, *Mycobacterium tuberculosis*, and proteopathic tau. During damage, mammalian ATG8s directly interacted with the core SG proteins NUFIP2 and G3BP1. Atg8ylation was needed for their recruitment to damaged lysosomes independently of SG condensates whereupon NUFIP2 contributed to mTOR inactivation via the Ragulator-RagA/B complex. Thus, cells employ membrane atg8ylation to control and coordinate SG and mTOR responses to lysosomal damage.

INTRODUCTION

The mammalian autophagy-related (ATG) factors participate in a number of processes including canonical (Morishita and Mizushima, 2019) and noncanonical autophagy (Galluzzi and Green, 2019) with implications in disease and physiology (Levine and Kroemer, 2019). These processes intersect with metabolic regulators, with signals transduced via phosphorylation by mTOR to the ATG apparatus through a module consisting of FIP200-ULK1-ATG13-ATG101 (Jia et al., 2018; Kim et al., 2011). ATGs participate in non-autophagic processes, e.g. ULK1 (mammalian ortholog of yeast Atg1) in glycolysis (Li et al., 2016) and disassembly of stress granules (SGs) (Wang et al., 2019). ATGs can play unique roles such as the mammalian ATG8 proteins (mATG8s) (Gu et al., 2019; Kumar et al., 2018), which can act even upstream of the lysosomally positioned regulators such as mTOR or TFEB (Kumar et al., 2020; Nakamura et al., 2020). These diverse responses include mATG8s' conjugation to various stressed or remodeling membranes via mATG8 lipidation or protein modifications (Carosi et al., 2021), collectively termed atg8ylation (Deretic and Lazarou, 2022).

Lysosomal damage elicits mobilization of ESCRT membrane repair systems (Skowyra et al., 2018), mTOR inactivation (Jia et al., 2018), the translocation of TFEB from lysosomes to the nucleus (Chauhan et al., 2016), ubiquitination response (Papadopoulos et al., 2017), AMPK activation (Jia et al., 2020a), lysophagy (Maejima et al., 2013), and lipid changes (Ellison et al., 2020). Since inactivation of mTOR (Shin and Zoncu, 2020), impacts multiple processes such as autophagy and protein translation, it is of interest to consider global changes in transcription and translation during lysosomal damage.

Stress granule (SG) formation is a part of global modulation of protein translation (Ivanov et al., 2019; Yang et al., 2020). SGs are cytoplasmic, membraneless liquid-liquid phase separated biomolecular condensates (Alberti et al., 2019) containing ribonucleoprotein particles (RNP), translational factors, the 40S ribosomal subunit (Kedersha et al., 2002), and a multitude of other proteins, e.g. G3BP1, TIA1, and NUFIP2 (Ivanov et al., 2019; Yang et al., 2020). Canonical SG formation depends on phosphorylation of eukaryotic translation initiation factor 2 α (eIF2 α), which blocks the assembly of productive translation preinitiation complexes (Kedersha et al., 1999). Heat shock, oxidative stress, hypoxia, and viral infections, are triggers of SG formation and translational arrest (Anderson and Kedersha, 2002). Mammalian eIF2 α is phosphorylated by four upstream kinases transducing stress, including PKR (Srivastava et al., 1998), PERK (Patil and Walter, 2001), GCN2 (Kimball, 2001), and HRI (McEwen et al., 2005).

Here we show that lysosomal damage is a previously unrecognized stressor eliciting canonical SG formation and translation changes. We report that atg8ylation (Deretic and Lazarou, 2022), a process that modifies stressed or remodeling membranes by lipid (Kumar et al., 2021b) or protein (Carosi et al., 2021) conjugation competes with SG formation. Based on proteomic approaches, we report that individual

SG proteins, NUFIP2 and G3BP1, which interact with mATG8s, are recruited to lysosomes and inactivate mTOR via the Ragulator-Rag system. These processes are elicited by lysosomal damaging agents including protopathic tau, *Mycobacterium tuberculosis*, and SARS-CoV-2^{ORF3a}.

RESULTS

Lysosomal proteome changes during lysosomal damage

To complement our studies of cellular homeostatic responses to lysosomal damage carried out by proximity biotinylation proteomics (Jia et al., 2018; Jia et al., 2020a; Jia et al., 2020b), here we carried out whole organelle proteomic analyses of normative and damaged lysosomes purified by LysoIP (Abu-Remaileh et al., 2017; Jia et al., 2020b) (Table S1, Tabs 1 and 2). We chose short pulse for lysosomal damage to capture early events minimizing more advanced degradative processes such as autophagy and other late-stage components of the MERiT response (Jia et al., 2020c). Cells were treated for 30 min with Leu-Leu-O-Me (LLOMe), which is a substrate by reverse peptidase reaction of cathepsin C resulting in growing polymers in the lysosomal lumen causing membrane damage and permeabilization (Thiele and Lipsky, 1990). Quantitative DIA proteomic analyses was carried out (Figure 1A; Table S1, Tabs 1 and 2 (i)) of damaged vs. undamaged lysosomes in HEK293T cells stably expressing TMEM192-3xHA following a well-established procedure for lysosomal purification (Jia et al., 2020a) (Figure 1A; Table S1, Tabs 1 and 2). The mass spectrometry data confirmed our prior observations (Jia et al., 2018) that mTOR and Raptor dissociate from lysosomes upon damage (Figure 1A) whereas STRING protein interaction network functional analysis (Szklarczyk et al., 2021) revealed enrichment of components of a number of biological processes including several previously not associated with lysosomal damage (Table S1, Tab 2 (ii) and (iii)).

As an independent control and measure of early cellular response to lysosomal injury, RNAseq analysis was carried out (Figure 2A; Table S1, Tab 3). RNAseq data revealed that during early lysosomal damage, several genes were induced including DUSP1 (Figure 2A). DUSP1 is a phosphatase inhibiting ERK2 activation (Kirk et al., 2020; Sun et al., 1993), whereas ERK2 is an upstream kinase for TFEB (Napolitano and Ballabio, 2016; Settembre et al., 2011). We tested DUSP1 protein levels and the status of ERK2 and TFEB and found: (i) that DUSP1 was increased (Figure 2B); (ii) that ERK2 was dephosphorylated (Figure 2B); (iii) that TFEB was dephosphorylated at its Ser142 residue, a known site for phosphorylation by ERK2 (Napolitano and Ballabio, 2016; Settembre et al., 2011) (Figure 2C); and (iv) that this depended on DUSP1 (Figure 2D). Finally, nuclear translocation of TFEB and dephosphorylation at Ser142 in response to lysosomal damage (Chauhan et al., 2016; Settembre et al., 2012) was observed at early time point and was equal in magnitude to the one caused by ERK2 inhibitor AZD6244 (Figures 2E, F). We conclude that early lysosomal damage and the chosen time point elicits a relevant cellular response consistent with prior observations (Jia et al., 2020b; Nakamura et al., 2020).

An abundance of ESCRT proteins was detected including ALIX (PDCD6IP) and TSG101, shown to contribute to lysosomal damage repair (Jia et al., 2020b; Radulovic et al., 2018; Skowrya et al., 2018) and all ESCRT-III components (Figure 1A, green; Table S1, Tab 4). Another category of proteins detected in DIA proteomic analysis of damaged lysosomes were autophagy-associated components (Figure 1A, blue; Table S1, Tab 5), with increase in ATG9A, MAP1LC3B, GABARAP, GABARAPL2, and ATG16L1. Thus, the global proteomic analysis was consistent with the ESCRT components being dynamically recruited and participating in repair of damaged lysosomes (Jia et al., 2020b; Skowrya et al., 2018). The evidence of autophagy factors gathering at the damaged lysosomes (Table S1, Tab 5) was consistent with prior studies (Eapen et al., 2021; Jia et al., 2020b; Maejima et al., 2013).

Proteomics of damaged lysosomes reveals connections to stress granule components

Our proteomic analyses of purified damaged lysosomes revealed abundance of proteins best known for their presence in stress granules (SGs) (Figure 1A, purple; Table S1, Tab 6). SGs are canonically induced in response to stressors such as heat shock (Nover et al., 1983), oxidative stress (Kedersha et al., 1999) and viral infection (Srivastava et al., 1998; Williams, 2001), however lysosomal damage has hitherto not been reported as an inducer of SGs. SG composition is complex and depending upon conditions and complementary genomic vs. proteomic approaches approach, can include 274 to 411 proteins (Jain et al., 2016; Yang et al., 2020). These sets of proteins include the proposed core of 36 SG proteins (Yang et al., 2020). Our LysolP proteomic analysis includes 32 out of the 36 core proteins (Table S1, Tab 6A). Of these, 20 showed statistically significant increase by quantitative DIA analysis (Figure 1A; Table S1, Tab 6A). Comparing our LysolP proteomic data with other summaries of proteins associated with SGs (Ivanov et al., 2019), we detected 13 additional exclusive SG proteins and 10 shared between SGs and P-bodies (Table S1, Tab 6B). Of these, 15 showed statistically significant increase by quantitative proteomics of damaged lysosomes (Figure 1A; Table S1, Tab 6B), for a total of 55 SG proteins in LysolP MS with 27 of those showing increased association with damaged lysosomes. SGs include stalled preinitiation complexes with 40S ribosomal subunit (Ivanov et al., 2019; Riggs et al., 2020). We detected 30 out of 33 human 40S proteins (Nakao et al., 2004) in our proteomic dataset, with 10 of those showing statistically significant increase in association with damaged lysosomes (Figure 1A; Table S1, Tab 6C). Thus, our quantitative proteomics analysis detected increased association of SG proteins with damaged lysosomes, including the conventional marker proteins for SGs, G3BP1 and TIA1 (Figure 1A) (Gilks et al., 2004; Kedersha et al., 2005). Another more recently widely accepted marker of SGs (Yang et al., 2020; Youn et al., 2018), NUFIP2, was prominent in our LysolP MS, and showed one of the highest enrichments upon lysosomal damage (Figure 1A). By LysolP immunoblotting, we confirmed that NUFIP2, G3BP1, and TIA1 are enriched on damaged lysosomes but not on lysosomes purified from cells treated with arsenite, a conventional inducer of SG formation response (Jain et al., 2016) (Figure S1A). We next tested whether SG proteins associated with

lysosomes are present on the surface or within the lysosomal lumen. NUFIP2 and G3BP1, like the regulator of mTOR LAMTOR1, were accessible to and degraded by proteinase K even without detergent treatment of LysolP preparations (Figure 1B). This was in contrast to LAMP2, which is mostly luminal with only its short C-terminal domain facing the cytosol (Figure 1B). Thus, NUFIP2 and G3BP1 were on the surface and not sequestered within the lumen of the lysosomes.

Using previously characterized G3BP1-GFP U2OS cells (Mackenzie et al., 2017), we further confirmed by proteomic and MS that G3BP1 is recruited to lysosomes upon damage but not under arsenite-treatment conditions in our experimental conditions. This is evidenced by G3BP1's interactions with LAMP1 and LAMP2 almost exclusively under lysosomal damage conditions (Table S1, Tabs 7 and 8). Thus, we conclude that proteins that are primarily known for being components of SGs are recruited to lysosomal membranes upon damage.

Lysosomal damage induces stress granule formation

We tested whether lysosomal damage induces SG formation using the conventional marker of SGs G3BP1 (Jain et al., 2016; Yang et al., 2020) in cell types amenable to high content microscopy (HCM) analysis (Claude-Taupin et al., 2021; Jia et al., 2018; Jia et al., 2020a; Jia et al., 2020b; Kumar et al., 2021a). In U2OS cells, the human osteosarcoma epithelial cell line that allows morphological analyses and is suitable for HCM, 30 min of LLOMe treatment caused morphologically detectable SGs (Figures 1C, D). This was quantified by HCM, indicating a robust SG formation response in cells subjected to lysosomal damage by LLOMe (Figure 1C). Unlike SG formation, LLOMe treatment did not elicit P-body formation in U2OS cells, as assessed by the DCP1a marker exclusive to P-bodies (Ivanov et al., 2019; Kedersha et al., 2005) (Figure S1B). A strong SG formation response was observed with GPN, another biochemical agent causing lysosomal damage (Berg et al., 1994; Jia et al., 2018) and in cells treated with agents such as silica crystals that physically damage lysosomal membranes (Hornung et al., 2008; Maejima et al., 2013) (Figure 1C). In contrast, starvation in EBSS, a common method of inducing autophagy or inhibiting mTOR (Deretic and Kroemer, 2021), did not cause SG response (Figure 1C) in keeping with a previous report (Prentzell et al., 2021). As another control for LLOMe, we used LOMe, a methoxy esterified leucine (instead of esterified Leu dipeptide) (Zoncu et al., 2011), and it did not induce SG formation (Figure 1C).

SG response was detected in other cells, including Huh7 cells, the human hepatocyte-derived carcinoma cell line (Figure S1C). SGs were detected in murine primary bone marrow derived macrophages (BMM) subjected to LLOMe treatment (Figure 1E). This response was as robust as a response to canonical SG inducer arsenite (Figure 1E). Arsenite however did not induce lysosomal damage, monitored by galectin-3 (Gal3) response, a conventional marker for lysosomal damage (Aits et al., 2015; Maejima et al., 2013) (Figure S1D). We confirmed SG response to lysosomal damage using another key immunofluorescence marker for SGs, TIA1 (Figures S1E, F). Further, we tested the effects of cycloheximide, as a known inhibitor of SG formation in

response to arsenite treatment by inhibiting translation elongation and freezing ribosomes on translating mRNAs (Freibaum et al., 2021; Kedersha et al., 2000). Cycloheximide caused similar reduction in SG formation whether cells were treated with LLOMe or with arsenite (Figures 1F, S1G (i)), whereas cycloheximide did not affect lysosomal damage monitored by Gal3 response (Figure S1G (ii, iii)). NUFIP2, G3BP1 and TIA1 were recruited to lysosomes independently of SG formation, since their enhanced levels in LysolP preparations from cells treated with LLOMe were not inhibited by cycloheximide (Figure 1G).

Activation of specific protein kinases has been established as a part of SG response, including eIF2 α (Kedersha et al., 1999). LLOMe treatment of U2OS cells for 30 min induced phosphorylation of eIF2 α on Ser51, whereas a recovery from lysosomal damage by LLOMe washout (Jia et al., 2020b; Maejima et al., 2013) subsided eIF2 α pS51 response (Figure S1H). This correlated with a reduction in the number of SGs upon LLOMe washout (Figure S1I). In BMMs subjected to lysosomal damage, the levels of eIF2 α pS51 were similar to those in cells treated with arsenite (Figure 1H). A similar increase in eIF2 α pS51 in response to LLOMe or arsenite was observed in HEK293T cells used in our proteomic studies (Figure S1J). In summary, based on the observed hallmarks of conventional SG response, we conclude that lysosomal damage is a newly identified noncanonical stimulus for induction of canonical SGs (Figure S1K). Lysosomal damage was upstream of SG formation, since a knockout of Gal3, in keeping with previous studies (Jia et al., 2020b) sensitized lysosomes to LLOMe-induced damage which was paralleled by increased SG formation in response to the same dose of LLOMe (Figure S1L).

The SGs monitored by G3BP1 puncta were authentic SGs as they completely overlapped with polyA RNA probe (Cy3-oligo-dT) detected by fluorescence in situ hybridization (FISH) (Figure 1I), since functional SGs sequester translationally arrested mRNAs (Anderson and Kedersha, 2006; Ivanov et al., 2019). The detected granules were authentic SGs since individual or double knockdowns of G3BP1 and G3BP2, by far the most critical scaffold factors for various SG inducing conditions, resulted in a reduction of detectable mRNA puncta per cell (Figure S1M). SGs contribute to stress-induced translation arrest which suppresses bulk cap-dependent protein synthesis, but enhances selective translation of ATF4 (Vattem and Wek, 2004), which is a part of integrated stress response (ISR) (Costa-Mattioli and Walter, 2020). We first tested whether LLOMe damage causes general translation shutdown using puromycin incorporation assay and found that LLOMe treatment caused general translational shutdown in a dose-dependent fashion (Figure 1J). Paralleling this mTOR was inhibited as measured by 4EBP1 phosphorylation (Figure 1K). However, ATF4 expression increased over time (Figure 1K). Increased ATF4 eventually leads to dephosphorylation of eIF2 α (Novoa et al., 2003), observed later during LLOMe treatment (Figure 1K). Thus, lysosomal damage elicits SGs and selective translation.

PKR transmits lysosomal damage signals leading to stress granule formation

How might lysosomal damage be perceived and relayed to the systems that regulate SG formation? Mammalian eIF2 α can be phosphorylated by four kinases (HRI, PKR, PERK and GCN2) relaying distinct stressors (McCormick and Khapersky, 2017; Riggs et al., 2020). In our proteomic analyses of purified damaged lysosomes, only PKR (10 unique peptides) was detected (Figure 3A). A trend in PKR increase upon damage was observed by quantitative DIA proteomic analysis of damaged vs. undamaged lysosomes (Figure 3A). Thus, we tested whether PKR and other eIF2 α kinases were required to transmit lysosomal damage and cause eIF2 α phosphorylation. Of the four tested, only a knockdown of PKR abrogated eIF2 α phosphorylation in response to lysosomal damage by LLOMe (Figure 3B). PKR was activated, as assessed by its phosphorylation at Thr446, in cells subjected to lysosomal damage (Figure 3C). An inhibitor of PKR, 2-aminopurine (2-AP) (Lu et al., 2012) inhibited eIF2 α phosphorylation in cells treated with LLOMe (Figure 3C). Thus, PKR is responsible for eIF2 α phosphorylation in response to lysosomal damage.

When we tested the effects of knockdowns of eIF2 α kinases on SG formation in response to lysosomal damage, only a knockdown of PKR showed statistically significant reduction in SG formation induced by LLOMe treatment (Figure 3D). Furthermore, 2-AP inhibited, in a dose-response fashion, SG formation in response to LLOMe treatment (Figure 3E). A more specific inhibitor of PKR, imidazo-oxindole C16, also reduced SG formation during lysosomal damage (Figure 3F). PKR recognizes dsRNA during viral infections (Williams, 2001). We thus tested the possibility that RNA potentially released from damaged lysosomes could activate PKR. We knocked down lysosomal RNase RNASET2 (Haud et al., 2011) but did not detect a reduction in SG formation in response to LLOMe (Figure S2A). Whereas the signaling details activating PKR during lysosomal damage remain to be defined, we nevertheless conclude that PKR, an upstream kinase regulating eIF2 α and SG formation, associates with lysosomes and that it is important in sensing lysosomal damage and transmitting damage-associated signals to the SG formation systems.

Stress granules induced by lysosomal damage show dynamic interactions with lysosomes

The SG core proteins NUFIP2, G3BP1 and TIA1 were recruited to lysosomes independently of SG condensate formation (Figure 1G) as described above in experiments where SG formation was inhibited by cycloheximide. Nevertheless, a question remained whether morphologically visible SGs induced by lysosomal damage associated with lysosomes? By confocal fluorescence microscopy, the majority of G3BP1-positive SGs formed during lysosomal damage were either independent of lysosomes or at best juxtaposed to lysosomes (Figure S2B). By HCM quantification, only a low number (10-20%) of SGs revealed by G3BP1 antibody or tagged NUFIP2 appeared associated with lysosomes 30 min after exposure to lysosomal damaging agent LLOMe (Figures S2C, D). Using live microscopy, we observed that the majority of SGs were forming in locations independent of lysosomes (Supplementary Movie 1; Figure S2E). Overall, the lysosomes and SGs appeared relatively static, albeit there were three types of dynamic events suggesting changing relationships vis-à-vis each

other (Supplementary Movies 2-4): (i) lysosomes and SGs remained independent of each other (Figure S2F(i)); (ii) SGs appeared to be associated with lysosomes initially but then separated (Figure S2F(ii)); and (iii) lysosomes and SGs started separately but then associated (Figure S2F(iii)). Thus, the majority of SGs as morphologically discernible profiles were separate from lysosomes.

NUFIP2 exits nucleus and localizes to lysosomes upon damage

Despite the separation between lysosomes and SGs as morphologically visualized profiles, our MS data with LysolIP indicated that certain protein components of SGs are enriched on damaged lysosomes. A top hit for this was NUFIP2 (Figure 1A), a widely appreciated component of SGs (Yang et al., 2020; Youn et al., 2018). We observed using confocal microscopy that NUFIP2 before LLOMe treatment was mostly in the nucleus of Huh7 cells, separated from the cytosolic G3BP1 (Figure S3A). Upon lysosomal damage, NUFIP2 translocated from the nucleus into the cytosol (Figure S3A), which was also observed by biochemically analyzing distribution in nuclear vs postnuclear cell lysate preparations (Figure S3C). A bioinformatics analysis of NUFIP2's primary structure, using consensus/algorithm (Kosugi et al., 2009) revealed a presence of a candidate nuclear localization signal (NLS) in NUFIP2 (Figure S3B). When we deleted the putative NLS in NUFIP2, NUFIP2 appeared absent in the nuclear fraction, i.e. was retained in the cytoplasm (Figure S3C). Since NUFIP2 WT was found on purified lysosomes only after lysosomal damage (Figure S1A), we wondered whether NUFIP2 Δ NLS would be by default on lysosomes. However, LysolIP analysis showed that NUFIP2 Δ NLS did not partition to lysosomes by default but also required additional signals generated during lysosomal damage to translocate to the lysosomes (Figure 4A). Thus, NUFIP2 translocates to lysosomes upon damage.

NUFIP2 contributes to mTOR inactivation during lysosomal damage

Recent studies have indicated that components of SGs, such as G3BP1 associated in earlier proteomic studies with NUFIP2 (Sowa et al., 2009), can reside on lysosomes, and have additional, noncanonical functions outside of the scope of SG formation, including effects on mTOR activity (Prentzell et al., 2021). A knockdown of NUFIP2 reduced mTOR desorption from the lysosomes (Figures S3D, E), which serves as a visual proxy for mTOR inactivation in response to various inputs including lysosomal damage (Jia et al., 2018). This was confirmed by testing phosphorylation of mTOR substrates, ULK1 (Ser757), S6K (Thr389) and 4EBP1 (Ser65), which was diminished in cells treated with LLOMe, but less so in cells knocked down for NUFIP2 (Figure S3F). We generated a CRISPR knockout of NUFIP2 in Huh7 cells (Huh7^{NUFIP2-KO}) (Figure S3G). The knockout was validated for its effects on SG formation in response to either canonical inducer arsenite or induction upon lysosomal damage, which were both reduced in Huh7^{NUFIP2-KO} cells (Figure 4B). mTOR in Huh7^{NUFIP2-KO} cells resisted inactivation in response to lysosomal damage, quantified by HCM of its desorption from lysosomes (Figures 4C, S3H). This was also reflected in levels of phospho-ULK1 (Ser757), phospho-S6K (Thr389), and phospho-4EBP1 (Ser65), which resisted reduction in Huh7^{NUFIP2-KO} cells, normally seen upon lysosomal damage (Jia et al.,

2018) (Figure 4D). This effect was specific for NUFIP2 as a knockdown of TIA1 did not affect inhibition of mTOR in response to LLOMe damage (Figure S3I). Treatment with a conventional catalytic inhibitor of mTOR, pp242, did not result in NUFIP2 recruitment to lysosomes (Figure 4E). NUFIP2 was recruited to damaged lysosomes even in cells expressing constitutively active RagB^{Q99L}, which maintains mTORC1 in active state (Figure 4E), indicating that NUFIP2 translocates to damaged lysosomes independently of mTOR activation state and is likely acting upstream of mTOR. Thus NUFIP2, a key protein classically associated with SGs, acts on lysosomes to inhibit mTOR during lysosomal damage.

Ragulator abundance and activity on damaged lysosomes is controlled by NUFIP2

We have previously shown that mTOR is inactivated during lysosomal damage via Ragulator-RagA/B system by the inactivation of Ragulator's GEF activity toward RagA/B, which in turn normally keep mTOR active (Jia et al., 2018). Our MS data of purified lysosomes after the damage revealed that four Ragulator components (LAMTOR1, 2, 3 and 5) were elevated on lysosomes (Figures 1A, 5A), which was confirmed for all Ragulator's components but was not observed for Rags by LysolP and Western blot analyses (Figures 5B, S3J). The increase in LAMTOR1 and decrease of mTOR on damaged lysosomes appeared abrogated in NUFIP2^{KO} cells (Figure 5C(i-iii)), whereas the total cellular levels of LAMTOR1 did not change (Figure 5C(iv)).

Activation state of the Ragulator can be assessed by increased interactions between LAMTOR2 (p14) and RagA when RagA is in its inactive, GDP-bound form (Bar-Peled et al., 2012; Jia et al., 2018). Using this established approach, we quantified complexes between RagA and LAMTOR2, and found them to be increased (reflecting inactive RagA state) during lysosomal damage, in keeping with our prior studies (Jia et al., 2018), but this was reduced in HEK293T cells stably expressing FLAG-LAMTOR2 knocked down for NUFIP2 (Figure 5D), indicating that NUFIP2 is required for inactivation of the Ragulator complex. Conversely, overexpression of NUFIP2 further increased the elevated association between FLAG-LAMTOR2 and endogenous RagA during lysosomal damage (Figure 5E). Thus, NUFIP2 is required for RagA inactivation. Furthermore, NUFIP2 was in complexes with LAMTOR1 (and other Ragulator components), but only under lysosomal damaging conditions (Figure 5F). We conclude that NUFIP2, a functional component of SGs (Yang et al., 2020) is also an important regulator of mTOR via Ragulator during lysosomal damage.

NUFIP2 and galectin-8 cooperate in mTOR response to lysosomal damage

The observation that NUFIP2 is a new regulator of mTOR prompted us to test the previously reported specific regulators of mTOR inactivation during lysosomal damage (Jia et al., 2018). TSC2 did not affect phosphorylation status of mTOR's substrates (Figure S3K), whereas RagB did, as expression of active RagB^{Q99L} (Jia et al., 2018) prevented loss of mTOR activity induced by LLOMe (Figure S3L), as previously reported for GPN damage (Jia et al., 2018). We next tested LGALS8 (galectin-8; Gal8),

the principal sensor transducing lysosomal damage to inhibit the Regulator-RagA/B system (Jia et al., 2018). Whereas Gal8 was needed to fully inhibit mTOR based on its retention on lysosomes in Gal8KO^{HeLa} cells exposed to LLOMe (Figure 6A), Gal8 had no effect on SG formation. G3BP1 puncta formed as robustly in Gal8KO^{HeLa} cells as in parental WT cells treated with LLOMe (Figure 6B).

We next examined relationships between NUFIP2, Gal8 and Regulator components. We found that Gal8 was required for inactivation of RagA by NUFIP2 in response to lysosomal damage by GPN (Figure 6C). Whereas the co-IP results (Figures 5E, F) indicated that NUFIP2 and all Regulator components (LAMTOR 1-5) can be in protein complexes, GST pulldowns indicated that these interactions were not direct (Figure 6D). Instead, we found that NUFIP2 interacted directly with Gal8 (Figures 6D, E, S3M). However, NUFIP2 recruitment to lysosomes surprisingly did not depend on Gal8 (Figure 6F), and thus other mechanisms for NUFIP2 translocation to lysosomes must be involved. Nevertheless, a model emerges whereby Gal8, which interacts directly with NUFIP2, transmits the effects of NUFIP2 to the Regulator-Rag complexes during mTOR inactivation early upon lysosomal damage.

Mammalian Atg8s participate in recruitment of NUFIP2 to damaged lysosomes

In a previous report (Markmiller et al., 2018) with arsenite induced SGs, proximity labeling of mATG8 proteins was reported when using G3BP1-APEX2. Thus, we considered the possibility that mATG8s, usually considered to function primarily in the process of clearance of damaged lysosomes in a process termed lysophagy (Maejima et al., 2013), could play an additional role in recruitment of SG proteins to damaged lysosomes. Our MS analysis revealed enrichment of GABARAP, GABARAPL2 and LC3B on damaged lysosomes (Figure 7A; Table S1, Tab 5). Among other autophagy factors increased on purified lysosomes after a short pulse (30 min) of LLOMe-induced damage were ATG16L1 and ATG9A (Figure 7A; Table S1, Tab 5), whereas other canonical autophagy factors were not enriched/responsive to lysosomal damage. We next tested whether mATG8s played a role in recruitment of SG proteins to damaged lysosomes. For this we compared the previously characterized (Gu et al., 2019; Nguyen et al., 2016) hexa^{KO} HeLa cell line with inactivated six mATG8s with its parental WT HeLa cell line. These cells expressing TMEM192-3xHA were treated with LLOMe and subjected to unbiased proteomic analysis of purified lysosomes. The volcano plot (Figure 7B) and data analyses (Table S1, Tab 9) indicated that NUFIP2 and G3BP1 were the only core SG proteins significantly increased on damaged lysosomes in WT HeLa cells compared to hexa^{KO} HeLa cells. This strongly suggests that mATG8s are the factors responsible for recruitment of these proteins (NUFIP2 and G3BP1) to damaged lysosomes. The uniqueness of NUFIP2 and G3BP1 among SG proteins in proteomic analyses of hexa^{KO} cells is in keeping with their recruitment being independent of SG condensates (Figure 1G).

Next, we used hexa^{KO} HeLa cells, LC3^{TKO} HeLa cells with inactivated three LC3s and GBRP^{TKO} HeLa cells with inactivated all three GABARAPs (Nguyen et al., 2016). The hexa^{KO} HeLa cells lost ability to recruit NUFIP2 and G3BP1 to damaged

lysosomes, as determined by Western blot analysis of lysosomes purified by LysolP (Figure 7C). The GABARAP subset of mATG8s was responsible for the recruitment of NUFIP2 and G3BP1, since LC3^{TKO} HeLa retained the ability to recruit NUFIP2 and G3BP1 whereas GBRP^{TKO} HeLa cells did not (Figure 7C). GABARAPs were also key for departure of mTOR and Raptor from damaged lysosomes (Figures 7C, S4A). LAMTOR1 (p18) and LAMTOR complex inversely mirrored mTOR by being enriched on damaged lysosomes (Figures 7C, S4A). LAMTOR1 enrichment on damaged lysosomes was lost in GBRP^{TKO} HeLa but not in LC3^{TKO} HeLa (Figure 7C). Thus, mATG8s, specifically GABARAPs, do not only function in autophagy, but have noncanonical roles in recruitment of NUFIP2 and G3BP1 to the lysosome upon damage.

GABARAPs interact directly with NUFIP2 and G3BP1

In GST pulldowns between NUFIP2 and a full panel of mATG8s and in parallel with G3BP1, GABARAP showed strong association with either of the proteins (Figures 7D-G). Some appreciable association was also observed with GABARAPL1 (Figures 7D-G). We also tested deletion constructs of NUFIP2 for their ability to bind GABARAP (Figure S4B). Deletion mapping of GABARAP domains required for interactions with NUFIP2 indicated that two epitopes, one N-terminally located and another one more centrally located (Figures 7H, S4C), suggesting that the binding site is not a single linear epitope, such as the previously reported LIR docking sites (LDS) or UIM-docking sites (UDS) (Johansen and Lamark, 2020; Marshall et al., 2019). Nevertheless, we tested single LDS (Y49A), UDS (F77A) and double LDS/UDS mutant GABARAP for binding to NUFIP2, and none of the mutations in these key residues defining LDS or UDS affected association with NUFIP2 in GST pulldowns (Figure S4D). Although the GST pulldown experiments clearly indicate that GABARAP and NUFIP2 noncovalently bind, we tested whether the newly described process of protein atg8ylation (Nguyen et al., 2021) may also take place between these two proteins. Using deca^{KO} HeLa cells lacking all ATG4s delipidating enzymes (which also act as peptidases/isopeptidases), transfected with HA-GABARAP-G (a derivative with the pre-exposed C-terminal Gly residue), we detected HA-GABARAP-atg8ylated form of NUFIP2 (but only in cells lacking ATG4s), as well as the expected non-covalently bound proteins in co-IPs (Figure S4E).

G3BP1 has recently been reported to associate with lysosomes (Prentzell et al., 2021) as also seen in our LysolP preparations (Figure 7C). G3BP1 association with damaged lysosomes depended on GABARAPs (Figure 7C). We thus tested whether G3BP1 can associate with mATG8s and found in GST pulldown assays that it interacted directly with GABARAP (Figures 7F, G). Furthermore, deletion mapping confirmed that the N-terminal region of GABARAP interacts with G3BP1 (Figures 7I, S4F, G). Individual or combined LDS and UDS mutants of GABARAP still bound G3BP1 (Figure S4D). Finally, NUFIP2 and G3BP1 directly (Figure S4H) and very strongly (with 60% of the input [³⁵S] Myc-G3BP1 being bound to its NUFIP2 partner (Figure S4I)) interacted with each other in GST pulldown experiments. This interaction was also observed in reverse pulldown experiments (Figure S4J). NUFIP2 strongly interacts with G3BP1 via G3BP1's N-terminal NTF2L domain (Figure S4K). G3BP1 and NUFIP2

constitutively interacted in co-IP experiments (Figure S4L). NUFIP2 recruitment to damaged lysosomes was independent of G3BP1 (Figure 6F), suggesting that the recruitment via direct interactions with GABARAP is a dominant process for NUFIP2's translocation to damaged lysosomes.

GABARAPs participate in mTOR inactivation but not in eIF2 α phosphorylation in response to lysosomal damage

Based on strong associations in functional and binding experiments between GABARAPs and NUFIP2 and the requirement for NUFIP2 in mTOR inactivation during lysosomal damage, we tested whether NUFIP2's interactors GABARAPs also played a role in mTOR inactivation. Using ULK1, S6K and 4EBP1 phosphorylation as a conventional measure of mTOR activity, we detected an expected drop in levels of S6K (Thr389), 4EBP1 (Ser65) and ULK1 (Ser757) phosphorylation upon lysosomal damage with LLOMe, a relationship that was preserved in LC3^{TKO} HeLa cells (Figures 8A, B(i-iii)). In contrast mTOR inactivation was not observed in hexa^{KO} and GBRP^{TKO} HeLa cells (Figures 8A, B(i-iii)). We next tested by HCM whether mTOR desorption from damaged lysosomes was affected by mATG8s. As with reduction in ULK1, S6K and 4EBP1 phosphorylation, mTOR association with lysosomes diminished upon lysosomal damage in WT and LC3^{TKO} HeLa cells but not as readily in hexa^{KO} and GBRP^{TKO} HeLa cells (Figures 8C, S4M).

We then wondered whether eIF2 α phosphorylation, which is a marker of canonical SG formation (Riggs et al., 2020) and is strongly induced by lysosomal damage (Figures 1H, S1H, J), might also be affected by GABARAPs. However, contrary to our expectations, the mATG8s subgroup or mATG8s as a whole were not affecting eIF2 α response to lysosomal damage (Figures 8A, B(iv)). This suggests a separation of functions of GABARAPs in mTOR inactivation vs. SG formation. In keeping with this interpretation, SG formation in response to lysosomal damage was only increased in hexa^{KO} and GBRP^{TKO} cells (Figure 8D). All three GABARAPs individually were capable of suppressing mTOR inactivation and SG formation in GBRP^{TKO} HeLa cells elicited by lysosomal damage (Figures S5A, B). In conclusion, GABARAPs control mTOR inactivation and independently affect SG levels by redistributing NUFIP2 to act upon Regulator and mTOR on damaged lysosomes

Atg8ylation plays a role in mTOR inhibition and competes with stress granule formation during lysosomal damage

Recently, the concept of atg8ylation has been introduced as a general membrane stress and remodeling response and a unifying mechanism for various roles of mATG8 lipidation in diverse processes beyond their conventional association with canonical autophagy (Deretic and Lazarou, 2022). Thus, we tested whether atg8ylation plays a role in mTOR inactivation by mATG8s, specifically GABARAPs, in conjunction with their binding partner NUFIP2. GABARAP was lipidated during LLOMe treatment (Figure S5C). Atg8ylation of damaged lysosomes was further documented by the lipidated form of GABARAP in LysolP preparations (Figures 1G, 4E) and by immunofluorescence

(Figure S5D). In pairwise comparisons with the atg8ylation (mATG8 lipidation) mutant ATG3^{KO} in Huh7 cells, ATG9A (Claude-Taupin et al., 2021), a canonical autophagy gene, did not affect either mTOR inactivation or SG formation in response to lysosomal damage, whereas ATG3^{KO} (Figure S5E) countered mTOR inactivation (quantified by HCM of mTOR desorption from lysosomes) and enhanced SG formation (Figures 9A, B, S5H). In another pairwise comparison between the atg8ylation mutant ATG16L1^{KO} and a canonical autophagy factor FIP200^{KO} (Figure S5F), ATG16L1^{KO} reduced mTOR inactivation and enhanced SG formation, whereas FIP200^{KO} did not (Figures 9C, D, S5I). In the last comparison employed between ATG3^{KO} (atg8ylation mutant) and ATG13^{KO} (canonical autophagy mutant) in HeLa cells (Figure S5G), the above relationships held up, i.e. ATG3^{KO} decreased mTOR inactivation and enhanced SG formation in response to lysosomal damage, whereas ATG13^{KO} did not (Figures 9E, F, S5J). In ATG3^{KO} and ATG16L1^{KO} cells, G3BP1 protein levels remained unchanged (Figure S5K). Knockdown of NUFIP2 in ATG3^{KO} cells did not further enhance the partial rescue of mTOR dissociation from lysosomes in ATG3^{KO} cells (Figure S5L), suggesting that atg8ylation and NUFIP2 act along the same pathway.

In conclusion, atg8ylation is important for mTOR inactivation during lysosomal damage, it antagonizes SG formation in response to the same stimulus, and competes for factors such as NUFIP2. The competition model (Figure 9G) is consistent with the absence of mATG8s' effects on eIF2 α phosphorylation during lysosomal damage.

Diverse pathological agents induce lysosomal damage and stress granule formation response

We tested whether the above molecular and cell biological processes associated with lysosomal damage are observed in cells affected by agents causing or modeling pathology and disease. *Mycobacterium tuberculosis* (*Mtb*) can permeabilize intracellular vacuoles in which it resides and affect the endolysosomal system in infected macrophages (Manzanillo et al., 2012) and cause lysosomal damage (Chauhan et al., 2016). Hence, we wondered whether virulent *Mtb* Erdman with its membrane penetrating and lysosomal damage capabilities can induce SGs upon infection of host cells. Murine bone marrow derived macrophages (BMMs) were infected with *Mtb* Erdman wild type and SG formation was quantified after 20 h of infection (Figure 10A). As a positive control for endomembrane damage we monitored the ubiquitin response (Chauhan et al., 2016; Yoshida et al., 2017), which paralleled that of SG formation (Figure 10A). In contrast, when BMMs were infected with *Mtb* Erdman mutant in ESX-1, a factor required for permeabilization of endomembranes by *Mtb* (Manzanillo et al., 2012), both SG formation and ubiquitin puncta formation response were diminished (Figure 10A). We further modeled events associated with phagocytosis of membrane permeabilizing bacteria using FuGENE HD-coated latex beads (with FuGENE HD used as a membrane damaging agent), and observed similar SG formation and ubiquitin puncta responses in U2OS cells (Figure 10B).

We and others have reported that proto-pathic tau induces lysosomal damage (Jia et al., 2020b; Papadopoulos et al., 2017). Treatment of U2OS cells with proto-pathic

tau (Jia et al., 2020b) induced both SG formation response and Gal3 puncta formation (Figure 10C), the latter being used as a lysosome damage marker (Aits et al., 2015).

Lastly, we tested a factor encoded by SARS-CoV-2, ORF3a. The corresponding ORF3a from SARS-CoV (SARS-CoV-1) is known to cause lysosomal damage (Yue et al., 2018) and evidence for reduced acidification of lysosomes with SARS-CoV-2^{ORF3a} has been presented (Ghosh et al., 2020). We generated a stable HeLa cell line with tetracycline controllable with Flp-In GFP-SARS-CoV-2^{ORF3a} (Figure S5M). Upon induction of SARS-CoV-2^{ORF3a} expression with tetracycline we observed SG formation and ubiquitin puncta response, a well-established marker of lysosomal damage (Papadopoulos et al., 2017), consistent with ORF3a causing lysosomal damage and that this in turn induces SG formation (Figure 10D). Thus, the relationships presented in this work are of relevance for multiple pathogenic insults of significance for major human diseases.

We carried out ORF3a interactome analysis by constructing HEK293T Flp-In^{TetON} GFP-SARS-CoV-2^{ORF3a} cells and carrying out DIA proteomic analysis with immunopurified GFP-ORF3a (Table S1, Tab 10). The HOPS component VPS39 was observed as one of the enriched ORF3a interactors in our proteomic study (Table S1, Tab 10). VPS39 has been reported in global SARS-CoV-2 interactome studies by others (Gordon et al., 2020; Stukalov et al., 2021). The effects of ORF3a on HOPS have also been validated in the context of lysosomal function within the autophagy pathway (Miao et al., 2021). STRING functional association protein networks analyses indicated 64 and 85 entries assigned to lysosomal membranes and lysosomes (Table S1, Tab 11). Among most abundant proteins found in our DIA proteomic analysis was GCN1, an upstream regulator of GCN2- eIF2 α - ATF4 axis during repression of global protein synthesis (Pochopien et al., 2021) (Table S1, Tab 10). We validated SARS-CoV2^{ORF3a} interaction with GCN1 in Co-IPs (Figures S5N, O). These analyses indicate that ORF3a imposes a concerted role on lysosomal function and host cell translational apparatus, which is reflected in the known effects of coronaviruses (Nakagawa et al., 2018) and SARS-CoV-2 (Gordon et al., 2020) on stress granule formation in host cells.

DISCUSSION

In this study we report that lysosomal damage induces SG formation as a part of cellular homeostatic responses to stressors. SG formation complements the reported mTOR inactivation during lysosomal damage (Eapen et al., 2021; Goodwin et al., 2021; Jia et al., 2018; Koerver et al., 2019). Together, SG formation and mTOR inhibition cover two key aspects of protein translation during stress (Costa-Mattioli and Walter, 2020; Lu et al., 2004). We found that mTOR inactivation and SG formation are coupled via GABARAPs and atg8ylation (Deretic and Lazarou, 2022).

The elements shared between SGs and mTOR regulation are the individual SG proteins NUFIP2 and G3BP1. They affect mTOR activity independently of SG condensates as demonstrated by cycloheximide experiments whereby SGs are not formed but NUFIP2 and G3BP1 are recruited to damaged lysosomes where they inhibit

mTOR. This role of NUFIP2 depends on atg8ylation and interactions with GABARAPs. Both NUFIP2, tested here, and G3BP1 reported elsewhere (Prentzell et al., 2021) play a role in inhibiting mTOR under different conditions through complementary mechanisms (Prentzell et al., 2021). The convergence of NUFIP2's and Gal8's actions upon mTOR integrates escalating signals during lysosomal damage, i.e. membrane stress leading to membrane atg8ylation (Deretic and Lazarou, 2022) and overt membrane damage with exposure of luminal glycans recognized by Gal8 (Jia et al., 2018).

G3BP1 is an essential component acting redundantly with G3BP2 in SG formation (Yang et al., 2020) whereas our quantitative data suggest that NUFIP2 affects how robust the SG formation is. Of significance, G3BP1 and NUFIP2 directly interact as established here in GST-pulldowns. Both proteins bind to GABARAPs, which may be essential for their function in mTOR inactivation. GABARAPs do not contribute to SG formation although they have been found in SGs (Markmiller et al., 2018).

The positive role of GABARAPs and atg8ylation in mTOR inactivation and their negative role in SG formation reflect a competition for a limited supply of GABARAPs balancing shutting down of the cap-dependent translation while favoring selective translation of stress response systems. Considering the canonical (McCormick and Khaperskyy, 2017) and noncanonical (Emara et al., 2012; Fujimura et al., 2012) types of SG responses, they may fit in the continuum of how cells balance mTOR inactivation with the eIF2 α phosphorylation.

As shown here, SARS-CoV-2^{ORF3a} induces SGs along with the lysosomal damage. SGs are of significance in viral infections (Lindquist et al., 2010; McCormick and Khaperskyy, 2017; Panas et al., 2012). Viral infections can activate PKR which phosphorylates eIF2 α (Srivastava et al., 1998) and trigger SG formation to inhibit viral translation (Balachandran et al., 2000; Williams, 2001). In our study, PKR was the key upstream kinase affecting eIF2 α phosphorylation in response to lysosomal damage and was at least in part on lysosomes. Our finding that virulent *Mtb* induces SG response in macrophages may be of relevance in pathogenesis of tuberculosis. SGs are a component of a broader integrated stress response ISR (Costa-Mattioli and Walter, 2020; Lu et al., 2004) whereas PKR-dependent eIF2 α phosphorylation (Lu et al., 2004) is an aspect of *Mtb* pathology in necrotic granulomas (Bhattacharya et al., 2021).

How PKR senses lysosomal perturbations remains to be determined. ATG16L1 is a key component of the E3 ligase driving membrane atg8ylation (Kumar et al., 2021b). ATG16L1 is known to interact with V-ATPase (Xu et al., 2019), however our proteomic data indicate synchronous reduction of V-ATPase subunits on lysosomes during early damage (Table S1, Tab 12). Alternatively, ATG16L1 can bind to ubiquitin (Fujita et al., 2013) and there is a strong ubiquitylation response associated with lysosomal damage (Papadopoulos et al., 2017). Additional work is needed to address the exact mechanism of ATG16L1 increase on damaged lysosomes.

In summary, GABARAPs and atg8ylation balance two important aspects of translational suppression via mTOR and SGs. Atg8ylation and mATG8s play a hitherto unrecognized function in the fine tuning of translational arrest at the interface with the ISR in cells exposed to sources of lysosomal stress in various disease and physiological conditions.

Acknowledgments

We thank K. Bhaskar for tau oligomers. This work was supported by NIH grants (R37AI042999 and R01AI111935) and a center grant (P20GM121176) to V. Deretic. The study was in part supported by a pilot award from the AIM center to J. Jia. Mass spectrometry analysis was supported by a NIH shared instrumentation grant S10OD021801 to B. Phinney. The authors declare no competing financial interests.

Authors contributions: J. Jia and V. Deretic conceptualized the study, designed the experiments and analyzed the data; J. Jia performed majority of the experiments; Z. B-hujabal and T. Johansen performed and interpreted GST pulldowns; M. Salemi, B. Phinney and L. Allers performed and interpreted mass spectrometry data; F. Wang, R. Peters, M. Mudd, T. Duque and R. Javed contributed experiments; V. Deretic wrote the manuscript with J. Jia's input. All authors read and reviewed the manuscript.

Declaration of Interests

The authors declare no competing interests.

REFERENCES

- Abu-Remaileh, M., Wyant, G.A., Kim, C., Laqtom, N.N., Abbasi, M., Chan, S.H., Freinkman, E., and Sabatini, D.M. (2017). Lysosomal metabolomics reveals V-ATPase- and mTOR-dependent regulation of amino acid efflux from lysosomes. *Science* *358*, 807-813.
- Aits, S., Krickler, J., Liu, B., Ellegaard, A.M., Hamalisto, S., Tvingsholm, S., Corcelle-Termeau, E., Hogh, S., Farkas, T., Holm Jonassen, A., *et al.* (2015). Sensitive detection of lysosomal membrane permeabilization by lysosomal galectin puncta assay. *Autophagy* *11*, 1408-1424.
- Alberti, S., Gladfelter, A., and Mittag, T. (2019). Considerations and challenges in studying liquid-liquid phase separation and biomolecular condensates. *Cell* *176*, 419-434.
- Anderson, P., and Kedersha, N. (2002). Stressful initiations. *Journal of cell science* *115*, 3227-3234.
- Anderson, P., and Kedersha, N. (2006). RNA granules. *Journal of Cell Biology* *172*, 803-808.
- Balachandran, S., Roberts, P.C., Brown, L.E., Truong, H., Pattnaik, A.K., Archer, D.R., and Barber, G.N. (2000). Essential role for the dsRNA-dependent protein kinase PKR in innate immunity to viral infection. *Immunity* *13*, 129-141.

Bar-Peled, L., Schweitzer, L.D., Zoncu, R., and Sabatini, D.M. (2012). Ragulator 1s a GEF for the Rag GTPases that Signal Amino Acid Levels to mTORC1. *Cell* 150, 1196-1208.

Berg, T.O., Stromhaug, E., Lovdal, T., Seglen, O., and Berg, T. (1994). Use of glycyl-L-phenylalanine 2-naphthylamide, a lysosome-disrupting cathepsin C substrate, to distinguish between lysosomes and prelysosomal endocytic vacuoles. *The Biochemical journal* 300 (Pt 1), 229-236.

Bhattacharya, B., Xiao, S., Chatterjee, S., Urbanowski, M., Ordonez, A., Ihms, E.A., Agrahari, G., Lun, S., Berland, R., Pichugin, A., *et al.* (2021). The integrated stress response mediates necrosis in murine Mycobacterium tuberculosis granulomas. *The Journal of clinical investigation* 131.

Carosi, J.M., Nguyen, T.N., Lazarou, M., Kumar, S., and Sargeant, T.J. (2021). ATG8ylation of proteins: A way to cope with cell stress? *The Journal of cell biology* 220.

Chauhan, S., Kumar, S., Jain, A., Ponpuak, M., Mudd, M.H., Kimura, T., Choi, S.W., Peters, R., Mandell, M., Bruun, J.A., *et al.* (2016). TRIMs and Galectins Globally Cooperate and TRIM16 and Galectin-3 Co-direct Autophagy in Endomembrane Damage Homeostasis. *Developmental cell* 39, 13-27.

Claude-Taupin, A., Jia, J., Bhujabal, Z., Garfa-Traore, M., Kumar, S., da Silva, G.P.D., Javed, R., Gu, Y., Allers, L., Peters, R., *et al.* (2021). ATG9A protects the plasma membrane from programmed and incidental permeabilization. *Nature cell biology*.

Costa-Mattioli, M., and Walter, P. (2020). The integrated stress response: From mechanism to disease. *Science* 368.

Deretic, V., and Kroemer, G. (2021). Autophagy in metabolism and quality control: opposing, complementary or interlinked functions? *Autophagy*, 1-10.

Deretic, V., and Lazarou, M. (2022). A guide to membrane atg8ylation and autophagy with reflections on immunity. *Journal of Cell Biology* *In press*.

Eapen, V.V., Swarup, S., Hoyer, M.J., Paulo, J.A., and Harper, W. (2021). Quantitative proteomics reveals the selectivity of ubiquitin-binding autophagy receptors in the turnover of damaged lysosomes by lysophagy. *eLife* 10, e72328.

Ellison, C.J., Kukulski, W., Boyle, K.B., Munro, S., and Randow, F. (2020). Transbilayer movement of sphingomyelin precedes catastrophic breakage of enterobacteria-containing vacuoles. *Current Biology* 30, 2974-2983. e2976.

Emara, M.M., Fujimura, K., Sciaranghella, D., Ivanova, V., Ivanov, P., and Anderson, P. (2012). Hydrogen peroxide induces stress granule formation independent of eIF2alpha phosphorylation. *Biochemical and biophysical research communications* 423, 763-769.

Freibaum, B.D., Messing, J., Yang, P., Kim, H.J., and Taylor, J.P. (2021). High-fidelity reconstitution of stress granules and nucleoli in mammalian cellular lysate. *Journal of Cell Biology* 220.

Fujimura, K., Sasaki, A.T., and Anderson, P. (2012). Selenite targets eIF4E-binding protein-1 to inhibit translation initiation and induce the assembly of non-canonical stress granules. *Nucleic acids research* 40, 8099-8110.

Fujita, N., Morita, E., Itoh, T., Tanaka, A., Nakaoka, M., Osada, Y., Umemoto, T., Saitoh, T., Nakatogawa, H., Kobayashi, S., *et al.* (2013). Recruitment of the autophagic machinery to endosomes during infection is mediated by ubiquitin. *The Journal of cell biology* 203, 115-128.

Galluzzi, L., and Green, D.R. (2019). Autophagy-Independent Functions of the Autophagy Machinery. *Cell* 177, 1682-1699.

Ghosh, S., Dellibovi-Ragheb, T.A., Kerviel, A., Pak, E., Qiu, Q., Fisher, M., Takvorian, P.M., Bleck, C., Hsu, V.W., Fehr, A.R., *et al.* (2020). beta-Coronaviruses Use Lysosomes for Egress Instead of the Biosynthetic Secretory Pathway. *Cell* 183, 1520-1535 e1514.

Gilks, N., Kedersha, N., Ayodele, M., Shen, L., Stoecklin, G., Dember, L.M., and Anderson, P. (2004). Stress granule assembly is mediated by prion-like aggregation of TIA-1. *Mol Biol Cell* 15, 5383-5398.

Goodwin, J., Walkup, W.G., Hooper, K., Li, T., Kishi-Itakura, C., Ng, A., Lehmborg, T., Jha, A., Kommineni, S., and Fletcher, K. (2021). GABARAP membrane conjugation sequesters the FLCN-FNIP tumor suppressor complex to activate TFEB and lysosomal biogenesis. *bioRxiv*.

Gordon, D.E., Jang, G.M., Bouhaddou, M., Xu, J., Obernier, K., White, K.M., O'Meara, M.J., Rezelj, V.V., Guo, J.Z., and Swaney, D.L. (2020). A SARS-CoV-2 protein interaction map reveals targets for drug repurposing. *Nature* 583, 459-468.

Gu, Y., Princely Abudu, Y., Kumar, S., Bissa, B., Choi, S.W., Jia, J., Lazarou, M., Eskelinen, E.L., Johansen, T., and Deretic, V. (2019). Mammalian Atg8 proteins regulate lysosome and autolysosome biogenesis through SNARE s. *The EMBO journal* 38, e101994.

Haud, N., Kara, F., Diekmann, S., Henneke, M., Willer, J.R., Hillwig, M.S., Gregg, R.G., MacIntosh, G.C., Gärtner, J., and Alia, A. (2011). *raset2* mutant zebrafish model familial cystic leukoencephalopathy and reveal a role for RNase T2 in degrading ribosomal RNA. *Proceedings of the National Academy of Sciences* 108, 1099-1103.

Hornung, V., Bauernfeind, F., Halle, A., Samstad, E.O., Kono, H., Rock, K.L., Fitzgerald, K.A., and Latz, E. (2008). Silica crystals and aluminum salts activate the NALP3 inflammasome through phagosomal destabilization. *Nature immunology* 9, 847-856.

Ivanov, P., Kedersha, N., and Anderson, P. (2019). Stress Granules and Processing Bodies in Translational Control. *Cold Spring Harb Perspect Biol* 11.

Jain, S., Wheeler, J.R., Walters, R.W., Agrawal, A., Barsic, A., and Parker, R. (2016). ATPase-Modulated Stress Granules Contain a Diverse Proteome and Substructure. *Cell* 164, 487-498.

Jia, J., Abudu, Y.P., Claude-Taupin, A., Gu, Y., Kumar, S., Choi, S.W., Peters, R., Mudd, M.H., Allers, L., Salemi, M., *et al.* (2018). Galectins Control mTOR in Response to Endomembrane Damage. *Molecular cell* 70, 120-135 e128.

Jia, J., Bissa, B., Brecht, L., Allers, L., Choi, S.W., Gu, Y., Zbinden, M., Burge, M.R., Timmins, G., Hallows, K., *et al.* (2020a). AMPK, a Regulator of Metabolism and Autophagy, Is Activated by Lysosomal Damage via a Novel Galectin-Directed Ubiquitin Signal Transduction System. *Molecular cell* 77, 951-969 e959.

Jia, J., Claude-Taupin, A., Gu, Y., Choi, S.W., Peters, R., Bissa, B., Mudd, M.H., Allers, L., Pallikkuth, S., Lidke, K.A., *et al.* (2020b). Galectin-3 Coordinates a Cellular System for Lysosomal Repair and Removal. *Developmental cell* 52, 69-87 e68.

Jia, J., Claude-Taupin, A., Gu, Y., Choi, S.W., Peters, R., Bissa, B., Mudd, M.H., Allers, L., Pallikkuth, S., Lidke, K.A., *et al.* (2020c). MERIT, a cellular system coordinating lysosomal repair, removal and replacement. *Autophagy* 16, 1539-1541.

Johansen, T., and Lamark, T. (2020). Selective Autophagy: ATG8 Family Proteins, LIR Motifs and Cargo Receptors. *Journal of molecular biology* 432, 80-103.

Kedersha, N., Chen, S., Gilks, N., Li, W., Miller, I.J., Stahl, J., and Anderson, P. (2002). Evidence that ternary complex (eIF2-GTP-tRNA(i)(Met))-deficient preinitiation complexes are core constituents of mammalian stress granules. *Mol Biol Cell* 13, 195-210.

Kedersha, N., Cho, M.R., Li, W., Yacono, P.W., Chen, S., Gilks, N., Golan, D.E., and Anderson, P. (2000). Dynamic shuttling of TIA-1 accompanies the recruitment of mRNA to mammalian stress granules. *The Journal of cell biology* 151, 1257-1268.

Kedersha, N., Stoecklin, G., Ayodele, M., Yacono, P., Lykke-Andersen, J., Fritzler, M.J., Scheuner, D., Kaufman, R.J., Golan, D.E., and Anderson, P. (2005). Stress granules and processing bodies are dynamically linked sites of mRNP remodeling. *The Journal of cell biology* 169, 871-884.

Kedersha, N.L., Gupta, M., Li, W., Miller, I., and Anderson, P. (1999). RNA-binding proteins TIA-1 and TIAR link the phosphorylation of eIF-2 alpha to the assembly of mammalian stress granules. *The Journal of cell biology* 147, 1431-1442.

Kim, J., Kundu, M., Viollet, B., and Guan, K.L. (2011). AMPK and mTOR regulate autophagy through direct phosphorylation of Ulk1. *Nature cell biology* 13, 132-141.

Kimball, S.R. (2001). Regulation of translation initiation by amino acids in eukaryotic cells. *Prog Mol Subcell Biol* 26, 155-184.

Kirk, S.G., Samavati, L., and Liu, Y. (2020). MAP kinase phosphatase-1, a gatekeeper of the acute innate immune response. *Life Sci* 241, 117157.

Koerver, L., Papadopoulos, C., Liu, B., Kravic, B., Rota, G., Brecht, L., Veenendaal, T., Polajnar, M., Bluemke, A., and Ehrmann, M. (2019). The ubiquitin-conjugating enzyme UBE2 QL1 coordinates lysophagy in response to endolysosomal damage. *EMBO reports* 20, e48014.

Kosugi, S., Hasebe, M., Tomita, M., and Yanagawa, H. (2009). Systematic identification of cell cycle-dependent yeast nucleocytoplasmic shuttling proteins by prediction of composite motifs. *Proceedings of the National Academy of Sciences* 106, 10171-10176.

Kumar, S., Jain, A., Choi, S.W., da Silva, G.P.D., Allers, L., Mudd, M.H., Peters, R.S., Anonsen, J.H., Rusten, T.E., Lazarou, M., *et al.* (2020). Mammalian Atg8 proteins and the autophagy factor IRGM control mTOR and TFEB at a regulatory node critical for responses to pathogens. *Nature cell biology* 22, 973-985.

Kumar, S., Jain, A., Farzam, F., Jia, J., Gu, Y., Choi, S.W., Mudd, M.H., Claude-Taupin, A., Wester, M.J., Lidke, K.A., *et al.* (2018). Mechanism of Stx17 recruitment to autophagosomes via IRGM and mammalian Atg8 proteins. *The Journal of cell biology* 217, 997-1013.

Kumar, S., Javed, R., Mudd, M., Pallikkuth, S., Lidke, K.A., Jain, A., Tangavelou, K., Gudmundsson, S.R., Ye, C., and Rusten, T.E. (2021a). Mammalian hybrid pre-autophagosomal structure HyPAS generates autophagosomes. *Cell* 184, 5950-5969. e5922.

Kumar, S., Jia, J., and Deretic, V. (2021b). Atg8ylation as a general membrane stress and remodeling response. *Cell Stress* 5, 128-142.

Levine, B., and Kroemer, G. (2019). Biological functions of autophagy genes: a disease perspective. *Cell* 176, 11-42.

Li, T.Y., Sun, Y., Liang, Y., Liu, Q., Shi, Y., Zhang, C.-S., Zhang, C., Song, L., Zhang, P., and Zhang, X. (2016). ULK1/2 constitute a bifurcate node controlling glucose metabolic fluxes in addition to autophagy. *Molecular cell* 62, 359-370.

Lindquist, M.E., Lifland, A.W., Utley, T.J., Santangelo, P.J., and Crowe, J.E., Jr. (2010). Respiratory syncytial virus induces host RNA stress granules to facilitate viral replication. *Journal of virology* 84, 12274-12284.

Lu, B., Nakamura, T., Inouye, K., Li, J., Tang, Y., Lundback, P., Valdes-Ferrer, S.I., Olofsson, P.S., Kalb, T., Roth, J., *et al.* (2012). Novel role of PKR in inflammasome activation and HMGB1 release. *Nature* 488, 670-674.

Lu, P.D., Jousse, C., Marciniak, S.J., Zhang, Y., Novoa, I., Scheuner, D., Kaufman, R.J., Ron, D., and Harding, H.P. (2004). Cytoprotection by pre-emptive conditional phosphorylation of translation initiation factor 2. *The EMBO journal* 23, 169-179.

Mackenzie, I.R., Nicholson, A.M., Sarkar, M., Messing, J., Purice, M.D., Pottier, C., Annu, K., Baker, M., Perkerson, R.B., and Kurti, A. (2017). TIA1 mutations in amyotrophic lateral sclerosis and frontotemporal dementia promote phase separation and alter stress granule dynamics. *Neuron* 95, 808-816. e809.

Maejima, I., Takahashi, A., Omori, H., Kimura, T., Takabatake, Y., Saitoh, T., Yamamoto, A., Hamasaki, M., Noda, T., Isaka, Y., *et al.* (2013). Autophagy sequesters damaged lysosomes to control lysosomal biogenesis and kidney injury. *The EMBO journal* 32, 2336-2347.

Manzanillo, P.S., Shiloh, M.U., Portnoy, D.A., and Cox, J.S. (2012). Mycobacterium Tuberculosis Activates the DNA-Dependent Cytosolic Surveillance Pathway within Macrophages. *Cell host & microbe* 11, 469-480.

Markmiller, S., Soltanieh, S., Server, K.L., Mak, R., Jin, W., Fang, M.Y., Luo, E.C., Krach, F., Yang, D., Sen, A., *et al.* (2018). Context-Dependent and Disease-Specific Diversity in Protein Interactions within Stress Granules. *Cell* 172, 590-604 e513.

Marshall, R.S., Hua, Z., Mali, S., McLoughlin, F., and Vierstra, R.D. (2019). ATG8-Binding UIM Proteins Define a New Class of Autophagy Adaptors and Receptors. *Cell* 177, 766-781 e724.

McCormick, C., and Khaperskyy, D.A. (2017). Translation inhibition and stress granules in the antiviral immune response. *Nat Rev Immunol* 17, 647-660.

McEwen, E., Kedersha, N., Song, B., Scheuner, D., Gilks, N., Han, A., Chen, J.J., Anderson, P., and Kaufman, R.J. (2005). Heme-regulated inhibitor kinase-mediated phosphorylation of eukaryotic translation initiation factor 2 inhibits translation, induces stress granule formation, and mediates survival upon arsenite exposure. *The Journal of biological chemistry* 280, 16925-16933.

Miao, G., Zhao, H., Li, Y., Ji, M., Chen, Y., Shi, Y., Bi, Y., Wang, P., and Zhang, H. (2021). ORF3a of the COVID-19 virus SARS-CoV-2 blocks HOPS complex-mediated assembly of the SNARE complex required for autolysosome formation. *Developmental cell* 56, 427-442. e425.

Morishita, H., and Mizushima, N. (2019). Diverse Cellular Roles of Autophagy. *Annu Rev Cell Dev Biol* 35, 453-475.

Nakagawa, K., Narayanan, K., Wada, M., and Makino, S. (2018). Inhibition of stress granule formation by Middle East respiratory syndrome coronavirus 4a accessory protein facilitates viral translation, leading to efficient virus replication. *Journal of virology* 92, e00902-00918.

Nakamura, S., Shigeyama, S., Minami, S., Shima, T., Akayama, S., Matsuda, T., Esposito, A., Napolitano, G., Kuma, A., and Namba-Hamano, T. (2020). LC3 lipidation is essential for TFEB activation during the lysosomal damage response to kidney injury. *Nature cell biology* 22, 1252-1263.

Nakao, A., Yoshihama, M., and Kenmochi, N. (2004). RPG: the Ribosomal Protein Gene database. *Nucleic acids research* 32, D168-170.

Napolitano, G., and Ballabio, A. (2016). TFEB at a glance. *Journal of cell science* 129, 2475-2481.

Nguyen, T.N., Padman, B.S., Usher, J., Oorschot, V., Ramm, G., and Lazarou, M. (2016). Atg8 family LC3/GABARAP proteins are crucial for autophagosome-lysosome fusion but not autophagosome formation during PINK1/Parkin mitophagy and starvation. *The Journal of cell biology* 215, 857-874.

Nguyen, T.N., Padman, B.S., Zellner, S., Khuu, G., Uoselis, L., Lam, W.K., Skulsupaisarn, M., Lindblom, R.S., Watts, E.M., and Behrends, C. (2021). ATG4 family proteins drive phagophore growth independently of the LC3/GABARAP lipidation system. *Molecular cell* 81, 2013-2030. e2019.

Nover, L., Scharf, K.D., and Neumann, D. (1983). Formation of cytoplasmic heat shock granules in tomato cell cultures and leaves. *Molecular and cellular biology* 3, 1648-1655.

Novoa, I., Zhang, Y., Zeng, H., Jungreis, R., Harding, H.P., and Ron, D. (2003). Stress-induced gene expression requires programmed recovery from translational repression. *The EMBO journal* 22, 1180-1187.

Panas, M.D., Varjak, M., Lulla, A., Eng, K.E., Merits, A., Karlsson Hedestam, G.B., and McInerney, G.M. (2012). Sequestration of G3BP coupled with efficient translation inhibits stress granules in Semliki Forest virus infection. *Mol Biol Cell* 23, 4701-4712.

Papadopoulos, C., Kirchner, P., Bug, M., Grum, D., Koerver, L., Schulze, N., Poehler, R., Dressler, A., Fengler, S., Arhzaouy, K., *et al.* (2017). VCP/p97 cooperates with YOD1, UBXD1 and PLAA to drive clearance of ruptured lysosomes by autophagy. *The EMBO journal* 36, 135-150.

Patil, C., and Walter, P. (2001). Intracellular signaling from the endoplasmic reticulum to the nucleus: the unfolded protein response in yeast and mammals. *Current opinion in cell biology* 13, 349-355.

Pochopien, A.A., Beckert, B., Kasvandik, S., Berninghausen, O., Beckmann, R., Tenson, T., and Wilson, D.N. (2021). Structure of Gcn1 bound to stalled and colliding 80S ribosomes. *Proceedings of the National Academy of Sciences* 118.

Prentzell, M.T., Rehbein, U., Sandoval, M.C., De Meulemeester, A.-S., Baumeister, R., Brohée, L., Berdel, B., Bockwoldt, M., Carroll, B., and Chowdhury, S.R. (2021). G3BPs tether the TSC complex to lysosomes and suppress mTORC1 signaling. *Cell* 184, 655-674. e627.

Radulovic, M., Schink, K.O., Wenzel, E.M., Nahse, V., Bongiovanni, A., Lafont, F., and Stenmark, H. (2018). ESCRT-mediated lysosome repair precedes lysophagy and promotes cell survival. *The EMBO journal* 37.

Riggs, C.L., Kedersha, N., Ivanov, P., and Anderson, P. (2020). Mammalian stress granules and P bodies at a glance. *Journal of cell science* 133.

Settembre, C., Di Malta, C., Polito, V.A., Garcia Arencibia, M., Vetrini, F., Erdin, S., Erdin, S.U., Huynh, T., Medina, D., Colella, P., *et al.* (2011). TFEB links autophagy to lysosomal biogenesis. *Science* 332, 1429-1433.

Settembre, C., Zoncu, R., Medina, D.L., Vetrini, F., Erdin, S., Erdin, S., Huynh, T., Ferron, M., Karsenty, G., and Vellard, M.C. (2012). A lysosome-to-nucleus signalling mechanism senses and regulates the lysosome via mTOR and TFEB. *The EMBO journal* 31, 1095-1108.

Shin, H.R., and Zoncu, R. (2020). The lysosome at the intersection of cellular growth and destruction. *Developmental cell*.

Skowyra, M.L., Schlesinger, P.H., Naismith, T.V., and Hanson, P.I. (2018). Triggered recruitment of ESCRT machinery promotes endolysosomal repair. *Science* 360.

Sowa, M.E., Bennett, E.J., Gygi, S.P., and Harper, J.W. (2009). Defining the human deubiquitinating enzyme interaction landscape. *Cell* 138, 389-403.

Srivastava, S.P., Kumar, K.U., and Kaufman, R.J. (1998). Phosphorylation of eukaryotic translation initiation factor 2 mediates apoptosis in response to activation of the double-stranded RNA-dependent protein kinase. *The Journal of biological chemistry* 273, 2416-2423.

Stukalov, A., Girault, V., Grass, V., Karayel, O., Bergant, V., Urban, C., Haas, D.A., Huang, Y., Oubraham, L., Wang, A., *et al.* (2021). Multilevel proteomics reveals host perturbations by SARS-CoV-2 and SARS-CoV. *Nature* 594, 246-252.

Sun, H., Charles, C.H., Lau, L.F., and Tonks, N.K. (1993). MKP-1 (3CH134), an immediate early gene product, is a dual specificity phosphatase that dephosphorylates MAP kinase in vivo. *Cell* 75, 487-493.

Szklarczyk, D., Gable, A.L., Nastou, K.C., Lyon, D., Kirsch, R., Pyysalo, S., Doncheva, N.T., Legeay, M., Fang, T., and Bork, P. (2021). The STRING database in 2021: customizable protein-protein networks, and functional characterization of user-uploaded gene/measurement sets. *Nucleic acids research* 49, D605-D612.

Thiele, D.L., and Lipsky, P.E. (1990). Mechanism of L-leucyl-L-leucine methyl ester-mediated killing of cytotoxic lymphocytes: dependence on a lysosomal thiol protease, dipeptidyl peptidase I, that is enriched in these cells. *Proceedings of the National Academy of Sciences of the United States of America* 87, 83-87.

Vattem, K.M., and Wek, R.C. (2004). Reinitiation involving upstream ORFs regulates ATF4 mRNA translation in mammalian cells. *Proceedings of the National Academy of Sciences* 101, 11269-11274.

Wang, B., Maxwell, B.A., Joo, J.H., Gwon, Y., Messing, J., Mishra, A., Shaw, T.I., Ward, A.L., Quan, H., Sakurada, S.M., *et al.* (2019). ULK1 and ULK2 Regulate Stress Granule Disassembly Through Phosphorylation and Activation of VCP/p97. *Molecular cell* 74, 742-757 e748.

Williams, B.R. (2001). Signal integration via PKR. *Sci STKE* 2001, re2.

Xu, Y., Zhou, P., Cheng, S., Lu, Q., Nowak, K., Hopp, A.-K., Li, L., Shi, X., Zhou, Z., and Gao, W. (2019). A bacterial effector reveals the V-ATPase-ATG16L1 axis that initiates xenophagy. *Cell* 178, 552-566. e520.

Yang, P., Mathieu, C., Kolaitis, R.M., Zhang, P., Messing, J., Yurtsever, U., Yang, Z., Wu, J., Li, Y., Pan, Q., *et al.* (2020). G3BP1 Is a Tunable Switch that Triggers Phase Separation to Assemble Stress Granules. *Cell* 181, 325-345 e328.

Yoshida, Y., Yasuda, S., Fujita, T., Hamasaki, M., Murakami, A., Kawawaki, J., Iwai, K., Saeki, Y., Yoshimori, T., Matsuda, N., *et al.* (2017). Ubiquitination of exposed glycoproteins by SCF(FBXO27) directs damaged lysosomes for autophagy. *Proceedings of the National Academy of Sciences of the United States of America* 114, 8574-8579.

Youn, J.Y., Dunham, W.H., Hong, S.J., Knight, J.D.R., Bashkurov, M., Chen, G.I., Bagci, H., Rathod, B., MacLeod, G., Eng, S.W.M., *et al.* (2018). High-Density Proximity Mapping Reveals the Subcellular Organization of mRNA-Associated Granules and Bodies. *Molecular cell* 69, 517-532 e511.

Yue, Y., Nabar, N.R., Shi, C.S., Kamenyeva, O., Xiao, X., Hwang, I.Y., Wang, M., and Kehrl, J.H. (2018). SARS-Coronavirus Open Reading Frame-3a drives multimodal necrotic cell death. *Cell death & disease* 9, 904.

Zoncu, R., Bar-Peled, L., Efeyan, A., Wang, S., Sancak, Y., and Sabatini, D.M. (2011). mTORC1 senses lysosomal amino acids through an inside-out mechanism that requires the vacuolar H(+)-ATPase. *Science* 334, 678-683.

Figure 1. Lysosomal damage induces stress granule formation. (A) EncyclopeDIA/scaffoldDIA LC/MS/MS quantitative analysis of proteins associated with lysosomes purified by LysolP (anti-HA immunoprecipitation) from HEK293T cells expressing TMEM192-3xHA untreated or treated with 1 mM LLOMe for 30 min. Three groups of proteins are denoted: ESCRT components, green; autophagy factors, blue; stress granule components, purple. Scatter (volcano) plot shows log₂ fold changes and -Log₁₀ p-values; n=3 (see Table S1, Tab 1). Dashed line, significance cut-off ($p < 0.05$). (B) Protease accessibility analysis of proteins associated with purified lysosomes (LysolP). Huh7 cells were treated with 2 mM LLOMe. LysolP preparations (treated or not with detergent Triton X-100) were digested with 30 μ g/mL proteinase K for 30 min and analyzed by immunoblotting. (C) Quantification by high-content microscopy (HCM) of G3BP1 puncta. U2OS cells were treated with EBSS, 4 mM LOME, 2 mM LLOMe, 200 μ M GPN, or 400 μ g/mL silica for 30 min. White masks, algorithm-defined cell boundaries (primary objects); red masks, computer-identified G3BP1 puncta (target objects). (D) Fluorescence confocal microscopy imaging of G3BP1. U2OS cells were treated with 2 mM LLOMe for 30 min and immunostained for endogenous G3BP1. Scale bar, 5 μ m. (E) Quantification by HCM of G3BP1 puncta in BMM (bone-marrow-derived macrophages) cells treated with 2 mM LLOMe or 100 μ M NaAsO₂ for 2 h. Green masks, computer-identified G3BP1 puncta. (F) Quantification by HCM of G3BP1 puncta in U2OS cells treated with LLOMe at indicated doses or 100 μ M NaAsO₂ in the presence or absence of 10 μ g/mL cycloheximide (CHX) for 30 min. HCM images in Figure S1G. (G) Analysis of proteins associated with purified lysosomes (LysolP; TMEM192-3xHA) from HEK293T cells treated with 2 mM LLOMe in the presence or absence of 10 μ g/mL cycloheximide (CHX) for 30 min. TMEM192-2xFLAG, control. (H) Immunoblot analysis of eIF2 α (S51) phosphorylation in BMM cells treated with 2 mM LLOMe or 100 μ M NaAsO₂ for 2h; eIF2 α p-S51 quantification, n=3. (I) Confocal microscopy analysis of G3BP1 (Alexa Fluor 488) and polyA RNA (Cy3-oligo[dT]) by fluorescence in situ hybridization (FISH) in U2OS cells treated with 2 mM LLOMe for 30 min. Scale bar, 5 μ m. (J) HCM analysis of protein synthesis using Click-iT™ Plus OPP Alexa Fluor™ 488 Protein Synthesis Assay (ThermoFisher) in U2OS cells treated with LLOMe at indicated doses or 100 μ M NaAsO₂ or 10 μ g/mL cycloheximide (CHX) for 30 min. (K) Immunoblot analysis of ATF4 and phosphorylation of 4EBP1 (S65) and eIF2 α (S51) in U2OS cells treated with 2 mM LLOMe for indicated time points; quantification of ATF4 and phosphorylation of 4EBP1 (S65) and eIF2 α (S51), n=3. Stress granules (SG). Ctrl, control (untreated cells). Data, means \pm SEM; HCM: n \geq 3 (each experiment: 500 valid primary objects/cells per well, \geq 5 wells/sample). † $p \geq 0.05$ (not significant), * $p < 0.05$, ** $p < 0.01$, ANOVA. See also Figure S1.

Figure 2. Cellular transcriptional response during lysosomal damage. (A) RNAseq analysis of the change in gene expression (HEK293T cells) in response to treatment with 1 mM LLOMe for 30 min. Scatter (volcano) plot shows log₂ fold change and -Log₁₀ p-value for the genes identified in three independent experiments (see Table S1, Tab 3). Red dots indicate the genes downregulated; green dots indicate the genes upregulated. Dashed line, significance cut-off ($p < 0.05$). (B) Immunoblot analysis of DUSP1 expression level and ERK2 (T185/187) phosphorylation in HEK293T cells treated with 1 mM LLOMe for 30 min. (C) Immunoblot analysis of TFEB (S142)

phosphorylation in U2OS cells treated with 2 mM LLOMe for 30 min. (D) Immunoblot analysis of ERK2 (T185/187) and TFEB (S142) phosphorylation in Huh7 cells transfected with scrambled siRNA as control (SCR) or DUSP1 siRNA treated with 2 mM LLOMe for 30 min. (E) Quantification by HCM of TFEB nuclear translocation in Huh7 cells treated with or without 530 nM ERK2 inhibitor AZD6244 for 2 h followed by 2 mM LLOMe for 30 min. Blue: nuclei, Hoechst 33342. Red: anti-TFEB antibody, Alexa Fluor 568. White masks, computer-algorithm-defined cell boundaries. Pink masks, computer-identified nuclear TFEB based on the average intensity of Alexa Fluor 568 fluorescence. (F) Immunoblot analysis of ERK2 (T185/187) and TFEB (S142) phosphorylation in Huh7 cells treated with or without 530 nM ERK2 inhibitor AZD6244 for 2 h followed by 2 mM LLOMe for 30 min. Ctrl, control (untreated cells). Data, means \pm SEM; HCM: $n \geq 3$ (each experiment: 500 valid primary objects/cells per well, ≥ 5 wells/sample). ** $p < 0.01$, ANOVA.

Figure 3. PKR transmits lysosomal damage signals leading to stress granule formation. (A) Unique PKR peptides and intensity (DIA); LysolP, $n=3$ (see Table S1, Tab 1). Mann-Whitney U test (LLOMe treatment relative to Ctrl). (B) Immunoblot analysis of the phosphorylation of eIF2 α (S51) in Huh7 cells transfected with scrambled siRNA as control (SCR) or HRI, PKR, PERK and GCN2 siRNA for knockdown (KD). Cells were treated with 2 mM LLOMe for 30 min. The level of phosphorylation of eIF2 α (S51) was quantified based on three independent experiments. (C) Immunoblot analysis of PKR (T446) and eIF2 α (S51) phosphorylation in U2OS cells treated with or without PKR inhibitor 2-Aminopurine (2-AP) for 1 h followed by 2 mM LLOMe treatment for 30 min as indicated. (D) Quantification by HCM of G3BP1 puncta in Huh7 cells transfected with scrambled siRNA as control (SCR) or HRI, PKR, PERK and GCN2 siRNA for knockdown (KD). Cells were treated with 2 mM LLOMe for 30 min. Red masks, computer-identified G3BP1 puncta. (E) Quantification by HCM of G3BP1 puncta in U2OS cells treated with or without PKR inhibitor 2-AP for 1 h followed by 2 mM LLOMe treatment for 30 min as indicated. (F) Quantification by HCM of G3BP1 puncta in U2OS cells treated with or without 210 nM imidazolo-oxindole C16 for 2 h followed by 2 mM LLOMe for 30 min. Red masks, computer-identified G3BP1 puncta. Ctrl, control (untreated cells). Data, means \pm SEM; HCM: $n \geq 3$ (each experiment: 500 valid primary objects/cells per well, ≥ 5 wells/sample). * $p < 0.05$, ** $p < 0.01$, ANOVA.

Figure 4. NUFIP2 contributes to mTOR inactivation during lysosomal damage. (A) Immunoblot analysis of FLAG-NUFIP2 or FLAG-NUFIP2 Δ NLS associated with purified lysosomes (LysolP; TMEM192-3xHA). Huh7 cells transfected with FLAG-NUFIP2 or FLAG-NUFIP2 Δ NLS, treated or not with 2 mM LLOMe for 30 min. TMEM192-2xFLAG, control. (B) Quantification by HCM of G3BP1 puncta in parental Huh7 (WT) and NUFIP2-knockout Huh7 cells (NUFIP2^{KO}) treated with 2 mM LLOMe or 100 μ M NaAsO₂ for 30 min. Red masks, computer-identified G3BP1 puncta. (C) Quantification by HCM of overlaps and confocal microscopy imaging of mTOR and LAMP2 in parental Huh7 (WT) and NUFIP2-knockout Huh7 cells (NUFIP2^{KO}) treated with 2 mM LLOMe for 30 min. HCM images in Figure S3H. Scale bar, 5 μ m. (D) Immunoblot analysis of indicated proteins in parental Huh7 (WT) and NUFIP2-knockout Huh7 cells (NUFIP2^{KO}) treated with 2 mM LLOMe for 30 min. The level of phosphorylation of ULK1 (S757), S6K (T389)

and 4EBP1 (S65) was quantified based on three independent experiments. (E) Immunoblot analysis of proteins associated with purified lysosomes (LysolP) from HEK293T cells treated with 1 μ M PP242 for 2 h or 2 mM LLOMe for 30 min or HEK293T cells stably expressing constitutively active RagB GTPase (RagB^{Q99L}) treated with 2 mM LLOMe for 30 min. Ctrl, control (untreated cells). Data, means \pm SEM; HCM: n \geq 3 (each experiment: 500 valid primary objects/cells per well, \geq 5 wells/sample). † p \geq 0.05 (not significant), *p < 0.05, **p < 0.01, ANOVA. See also Figure S3.

Figure 5. Regulator abundance and activity on damaged lysosomes is controlled by NUFIP2. (A) Summary of the relevant proteins of mTORC1 signaling in EncyclopeDIA/scaffoldDIA LysolP LC/MS/MS analysis. Fold change (FC). (see STAR methods, and Table S1, Tab 1). (B) Immunoblot analysis of proteins associated with purified lysosomes (LysolP; TMEM192-3xHA) from HEK293T cells treated with 2 mM LLOMe for 30 min. TMEM192-2xFLAG, control. (C) Immunoblot analysis of proteins associated with purified lysosomes (LysolP) from parental Huh7 WT and NUFIP2-knockout Huh7 cells (NUFIP2^{KO}) treated with 2 mM LLOMe for 30 min (i); quantification (ii-iv), n=3. (D) HEK293T cells stably expressing FLAG-Metap2 (control) or FLAG-LAMTOR2 transfected with scrambled siRNA (SCR) or NUFIP2 siRNA (NUFIP2^{KD}) were treated with 2 mM LLOMe for 30 min. Cell lysates were immunoprecipitated (IP) with anti-FLAG antibody and immunoblotted for indicated proteins. Quantification of interaction between RagA and LAMTOR2, n=3. (E) HEK293T cells stably expressing FLAG-Metap2 (control) or FLAG-LAMTOR2 transfected with GFP or GFP-NUFIP2 were treated with 2 mM LLOMe for 30 min. Cell lysates were immunoprecipitated (IP) with anti-FLAG antibody and immunoblotted for indicated proteins. Quantification of interaction between RagA and LAMTOR2, n=3. (F) HEK293T cells expressing FLAG (control) or FLAG-NUFIP2 were treated with 2 mM LLOMe for 30 min. Cell lysates were immunoprecipitated (IP) with anti-FLAG antibody and immunoblotted for indicated proteins. Data, means \pm SEM; † p \geq 0.05 (not significant), *p < 0.05, **p < 0.01, ANOVA. See also Figure S3.

Figure 6. NUFIP2 and galectin-8 cooperate in mTOR response to lysosomal damage. (A) Quantification by HCM of overlaps between mTOR and LAMP2 in Gal8WT^{HeLa} (WT) or Gal8KO^{HeLa} (Gal8^{KO}) cells treated with 2 mM LLOMe for 30 min. Yellow masks, computer-identified overlap of mTOR and LAMP2. (B) Quantification by HCM of G3BP1 puncta in Gal8WT^{HeLa} (WT) or Gal8KO^{HeLa} (Gal8^{KO}) cells treated with 2 mM LLOMe for 30 min. Red masks, computer-identified G3BP1 puncta. (C) HEK293T cells stably expressing FLAG-LAMTOR2 with overexpression of GFP or GFP-NUFIP2 were transfected with scrambled siRNA as control (SCR) or galectin-8 siRNA (Gal8^{KD}). Cells were treated with 200 μ M GPN for 30 min. Cell lysates were immunoprecipitated (IP) with anti-FLAG antibody and immunoblotted for indicated proteins. (D) GST pull-down assay of *in vitro* translated and radiolabeled Myc-tagged NUFIP2 or G3BP1 with GST or GST-tagged Regulator or galectin-8. (E) GST pull-down assay of *in vitro* translated and radiolabeled Myc-tagged NUFIP2 with GST or GST-tagged galectin-8. Quantification, n=3. (F) Analysis of indicated proteins associated with lysosomes purified by anti-HA immunoprecipitation (LysolP; TMEM192-3xHA) from HeLa WT, galectin-8 knockout (Gal8^{KO}), GABARAPs knockout (GBRP^{TKO}) or G3BP1 knockdown

(G3BP1^{KD}) cells. Cells were treated with 200 μ M GPN for 30 min. Autoradiography (AR). Ctrl, control (untreated cells). Data, means \pm SEM; HCM: $n \geq 3$ (each experiment: 500 valid primary objects/cells per well, ≥ 5 wells/sample). † $p \geq 0.05$ (not significant), ** $p < 0.01$, ANOVA. See also Figure S3.

Figure 7. Mammalian Atg8s participate in recruitment of NUFIP2 to damaged lysosomes. (A) Summary of the relevant proteins of autophagy factors in EncyclopeDIA/scaffoldDIA LC/MS/MS analysis of LysolP in HEK293T cells (see STAR methods, and Table S1, Tab 5). Fold change (FC). (B) EncyclopeDIA/scaffoldDIA LC/MS/MS analysis of lysosomes purified by anti-HA immunoprecipitation (LysolP; TMEM192-3xHA) from parental HeLa wildtype (HeLa^{WT}) or mATG8 knockout (hexa^{KO}) treated with or without 4 mM LLOMe for 30 min. Scatter (volcano; log₂ fold change and -Log₁₀ p-values) plot of stress granule core proteins; $n=3$ (see Table S1, Tab 9). Dashed line, significance cut-off ($p < 0.05$). (C) Analysis of indicated proteins associated with purified lysosomes. Lysosomes were purified by anti-HA immunoprecipitation (LysolP; TMEM192-3xHA) from parental HeLa (WT), LC3^{TKO}, GBRP^{TKO} and hexa^{KO} cells treated with 4 mM LLOMe for 30 min. (D) GST pull-down assay of *in vitro* translated and radiolabeled Myc-tagged NUFIP2 with GST or GST-tagged mATG8. GABARAP(GABA); GABARAPL1(GABAL1); GABARAPL2 (GABAL2). (E) Quantification of Figure 7D. Data (% binding) represents the percentage of the corresponding protein relative to its input. (F) GST pull-down assay of *in vitro* translated and radiolabeled Myc-tagged G3BP1 with GST or GST-tagged mATG8. GABARAP(GABA); GABARAPL1(GABAL1); GABARAPL2 (GABAL2). (G) Quantification of Figure 7F. Data (% binding) represents the percentage of the corresponding protein relative to its input. (H) Quantification of GST pull-down assay of *in vitro* translated and radiolabeled Myc-tagged NUFIP2 with GST or GST-tagged GABARAP deletions. Blots in Figure S4C. Data (% binding) represents the percentage of the corresponding protein relative to its input. (I) Quantification of GST pull-down assay of *in vitro* translated and radiolabeled Myc-tagged G3BP1 with GST or GST-tagged GABARAP deletions. Blots in Figure S4F. Data (% binding) represents the percentage of the corresponding protein relative to its input. Data, means \pm SEM; † $p \geq 0.05$ (not significant), * $p < 0.05$, ** $p < 0.01$, ANOVA. See also Figure S4.

Figure 8. GABARAPs participate in mTOR inactivation but not in eIF2 α phosphorylation in response to lysosomal damage. (A) Immunoblot analysis of the phosphorylation ULK1 (S757), S6K (T389), 4EBP1 (S65) and eIF2 α (S51) in parental HeLa (WT), LC3^{TKO}, GBRP^{TKO} and hexa^{KO} cells treated with 4 mM LLOMe for 30 min. (B) Quantification of phosphorylation of ULK1 (S757) (i), S6K (T389) (ii), 4EBP1 (S65) (iii) and eIF2 α (S51) (iv) in Figure 8A; Quantification, $n=3$. (C) Quantification by HCM and confocal microscopy analysis of overlaps between mTOR and LAMP2 in parental HeLa (WT), LC3^{TKO}, GBRP^{TKO} and hexa^{KO} cells treated with 4 mM LLOMe for 30 min. HCM images in Figure S4M. Scale bar, 5 μ m. (D) Quantification by HCM of G3BP1 puncta. Parental HeLa (WT), LC3^{TKO}, GBRP^{TKO} and hexa^{KO} cells were treated with 4 mM LLOMe for 30 min. Red masks, computer-identified G3BP1 puncta. Data, means \pm SEM; HCM: $n \geq 3$ (each experiment: 500 valid primary objects/cells per well, ≥ 5 wells/sample). † $p \geq 0.05$ (not significant), ** $p < 0.01$, ANOVA. See also Figure S4.

Figure 9. Atg8ylation plays a role in mTOR inhibition and competes with stress granule formation during lysosomal damage. (A) Quantification by HCM and confocal microscopy imaging of overlaps between mTOR and LAMP2 in parental Huh7(WT), ATG9^{KO} and ATG3^{KO} treated with 2 mM LLOMe for 30 min. HCM images in Figure S5H. Scale bar, 5 μ m. (B) Quantification by HCM of G3BP1 puncta. Parental Huh7(WT), ATG9^{KO} and ATG3^{KO} were treated with 2 mM LLOMe for 30 min. White masks, algorithm-defined cell boundaries. Red masks, computer-identified G3BP1 puncta. (C) Quantification by HCM and confocal microscopy imaging of overlaps between mTOR and LAMP2 in parental Huh7(WT), FIP200^{KO} and ATG16L1^{KO} treated with 2 mM LLOMe for 30 min. HCM images in Figure S5I. Scale bar, 5 μ m. (D) Quantification by HCM of G3BP1 puncta. Parental Huh7(WT), FIP200^{KO} and ATG16L1^{KO} were treated with 2 mM LLOMe for 30 min. Red masks, computer-identified G3BP1 puncta. (E) Quantification by HCM and confocal microscopy imaging of overlaps between mTOR and LAMP2 in parental HeLa (WT), ATG13^{KO} and ATG3^{KO} treated with 4 mM LLOMe for 30 min. HCM images in Figure S5J. Scale bar, 5 μ m. (F) Quantification by HCM of G3BP1 puncta. Parental HeLa (WT), ATG13^{KO} and ATG3^{KO} were treated with 4 mM LLOMe for 30 min. Red masks, computer-identified G3BP1 puncta. (G) Schematic summary of the findings in this study. Ctrl, control (untreated cells). Data, means \pm SEM; HCM: $n \geq 3$ (each experiment: 500 valid primary objects/cells per well, ≥ 5 wells/sample). † $p \geq 0.05$ (not significant), ** $p < 0.01$, ANOVA. See also Figure S5.

Figure 10. Diverse pathological agents induce lysosomal damage and stress granule formation response. (A) Quantification by HCM of G3BP1 and ubiquitin (Ubi) puncta in BMM cells infected with *Mtb* strain Erdman or its ESX-1 mutant at MOI = 10 for 20 h. White masks, algorithm-defined cell boundaries. Red masks, computer-identified G3BP1 puncta. Green masks, computer-identified ubiquitin puncta. (B) Quantification by HCM of G3BP1 and ubiquitin (Ubi) puncta in U2OS cells treated with FuGENE HD-coated latex beads (Polybead Amino Microsphere) for 16 h. Green masks, computer-identified G3BP1 puncta. Red masks, computer-identified ubiquitin puncta. (C) Quantification by HCM of G3BP1 and galectin-3 (Gal3) puncta in U2OS cells treated with 1 or 10 μ g/mL Tau oligomer overnight. Red masks, computer-identified G3BP1 puncta. Green masks, computer-identified Gal3 puncta. (D) Quantification by HCM of G3BP1 and ubiquitin (Ubi) puncta in the constructed HeLa Flp-In^{TetON} GFP-SARS-CoV-2^{ORF3a} cells induced by 1 μ g/mL tetracycline (Tet). Red masks, computer-identified G3BP1 puncta. Pink masks, computer-identified ubiquitin puncta. Stress granules (SG). Data, means \pm SEM; HCM: $n \geq 3$ (each experiment: 500 valid primary objects/cells per well, ≥ 5 wells/sample). † $p \geq 0.05$ (not significant), * $p < 0.05$, ** $p < 0.01$, ANOVA. See also Figure S5.

Figure S1. Stress granule formation during lysosomal damage. (A) Immunoblot analysis of proteins associated with purified lysosomes (LysolP; anti-HA immunoprecipitation TMEM192^{3xHA}) from HEK293T cells treated with 2 mM LLOMe or 100 μ M NaAsO₂ for 30 min. TMEM192^{2xFLAG}, control. (B) Quantification by HCM of DCP1a and G3BP1 puncta in U2OS cells treated with 2 mM LLOMe for 30 min. P-body

(PB). Stress granules (SG). (C) Quantification by HCM of G3BP1 puncta in Huh7 cells treated with 2 mM LLOMe for 30 min. White masks, algorithm-defined cell boundaries (primary objects); Green masks, computer-identified G3BP1 puncta (target objects). (D) Quantification by HCM of galectin-3 puncta in BMM cells treated with 2 mM LLOMe or 100 μ M NaAsO₂ for 2h. Red masks, computer-identified galectin-3 puncta. (E) Quantification by HCM of TIA1 puncta in U2OS cells treated with 2 mM LLOMe for 30 min. Red masks, computer-identified TIA1 puncta. (F) Quantification by HCM of TIA1 puncta in HeLa cells treated with 4 mM LLOMe for 30 min. Red masks, computer-identified TIA1 puncta. (G) Quantification by HCM of G3BP1 and galectin-3 puncta in U2OS cells treated with increasing doses of LLOMe or 100 μ M NaAsO₂ in the presence or absence of 10 μ g/mL cycloheximide (CHX) for 30 min. (i) HCM sample images corresponding to Figure 1F. Red masks, computer-identified G3BP1 puncta. (ii) Green masks, computer-identified galectin-3 (Gal3) puncta and corresponding quantification in (iii). (H) Immunoblot analysis of eIF2 α (S51) phosphorylation in U2OS cells treated with 2 mM LLOMe for 30 min and followed by 1 h washout. (I) Quantification by HCM of G3BP1 puncta in U2OS cells treated with 2 mM LLOMe for 30 min and followed by 1h washout. Red masks, computer-identified G3BP1 puncta. (J) Immunoblot analysis of eIF2 α (S51) phosphorylation in HEK293T cells treated with 2 mM LLOMe or 100 μ M NaAsO₂ for 30 min. (K) Schematic summary of the findings in Figure 1. (L) Quantification by HCM of LysoTracker Red (LTR) and G3BP1 puncta in parental HeLa wildtype (WT) and galectin-3 knockout (Gal3^{KO}) cells treated with 4 mM LLOMe for 30 min. Red masks, computer-identified LTR puncta. Green masks, computer-identified G3BP1 puncta. (M) Quantification by HCM of polyA RNA (Cy3-oligo[dT]) in U2OS cells transfected with scrambled siRNA as control (SCR) or G3BP1/2 siRNA for single or double knockdown (DKD). Cells were treated with 2 mM LLOMe for 30 min. Red masks, computer-identified polyA RNA puncta. Ctrl, control (untreated cells). Data, means \pm SEM; HCM: n \geq 3 (each experiment: 500 valid primary objects/cells per well, \geq 5 wells/sample). † p \geq 0.05 (not significant), **p < 0.01, ANOVA. See also Figure 1.

Figure S2. Stress granules induced by lysosomal damage show limited and dynamic interactions with lysosomes. (A) Quantification by HCM of G3BP1 puncta in Huh7 cells transfected with scrambled siRNA as control (SCR) or RNASET2 siRNA treated with 2 mM LLOMe for 30 min. Red masks, computer-identified G3BP1 puncta. (B) Immunofluorescence confocal microscopy analysis of G3BP1 and LAMP2. U2OS cells were treated with 2 mM LLOMe for 30 min and stained for endogenous G3BP1 and LAMP2. Scale bar, 5 μ m. (C) Quantification by HCM of overlaps between G3BP1 and LAMP2 in U2OS cells treated with 2 mM LLOMe for 30 min. White masks, algorithm-defined cell boundaries. Yellow masks, computer-identified overlap of G3BP1 and LAMP2. (D) Quantification by HCM of overlaps between FLAG-NUFIP2 and LAMP2 in U2OS cells expressing FLAG-NUFIP2 treated with 2 mM LLOMe for 30 min. Yellow masks, computer-identified overlap of FLAG-NUFIP2 and LAMP2. (E) Still frames from live-cell fluorescence imaging analysis of mCherry-G3BP1 and GFP-LAMP1. U2OS cells expressing mCherry-G3BP1 and GFP-LAMP1 were incubated with 2 mM LLOMe during live-cell fluorescence imaging. Arrows, the representative regions at indicated timepoint. (F) Zoom views of regions in panel E. Ctrl, control (untreated cells). Data,

means \pm SEM; HCM: $n \geq 3$ (each experiment: 500 valid primary objects/cells per well, ≥ 5 wells/sample). ** $p < 0.01$, ANOVA.

Figure S3. NUFIP2 exits nucleus and localizes to lysosomes upon damage and cooperates with galectin-8 in mTORC1 response to lysosomal damage. (A) Immunofluorescence confocal microscopy analysis of G3BP1 and NUFIP2. Huh7 cells were treated with 2 mM LLOMe for 30 min and stained for endogenous G3BP1 and NUFIP2. Scale bar, 5 μ m. (B) The NLS (nuclear localization signal) analysis of NUFIP2 by cNLS Mapper. The sequence in red, predicted NLS in NUFIP2, was deleted for generating NUFIP2 Δ NLS. (C) Immunoblot analysis of NUFIP2 distribution in nuclear or postnuclear of Huh7 cells transfected with FLAG-NUFIP2 or NUFIP2 Δ NLS after the treatment with 2 mM LLOMe for 30 min. Confocal microscopy analysis (D) and quantification by HCM (E) of overlaps between mTOR and LAMP2 in U2OS transfected with scrambled siRNA as control (SCR) or NUFIP2 siRNA (NUFIP2KD) treated with 2 mM LLOMe for 30 min. Scale bar, 5 μ m. (F) Immunoblot analysis of indicated proteins in U2OS cells transfected with scrambled siRNA as control (SCR) or NUFIP2 siRNA (NUFIP2KD) treated with 2 mM LLOMe for 30 min. The level of phosphorylation of ULK1 (S757), S6K (T389) and 4EBP1 (S65) was quantified based on three independent experiments. (G) Immunoblot validation of NUFIP2-knockout in Huh7 cells. #E7 was used in the following experiments, named as Huh7^{NUFIP2-KO}. (H) HCM images of Figure 4C. Yellow masks, computer-identified overlap of mTOR and LAMP2. (I) Immunoblot analysis of indicated proteins in Huh7 cells transfected with scrambled siRNA as control (SCR) or TIA1 siRNA (TIA1^{KD}) treated with 2 mM LLOMe for 30 min. (J) Analysis of indicated proteins associated with lysosomes purified by anti-HA immunoprecipitation (LysolP; TMEM192-3xHA) from HEK293T cells treated with 2 mM LLOMe for 30 min. TMEM192-2xFLAG, control. (K) Immunoblot analysis of the phosphorylation of ULK1 (S757), S6K1 (T389) and 4EBP1 (S65) in parental HeLa (WT) and TSC2-knockout HeLa cells (TSC2^{KO}) treated with 2 mM LLOMe for 30 min. (L) Immunoblot analysis of the phosphorylation of ULK1 (S757), S6K1 (T389) and 4EBP1 (S65) in HEK293T cells or HEK293T cells stably expressing constitutively active RagB GTPase (RagB^{Q99L}) treated with 2 mM LLOMe for 30 min. (M) GST pull-down assay of *in vitro* translated and radiolabeled Myc-tagged NUFIP2 or G3BP1 with GST or GST-tagged galectin-8 (Gal8). Autoradiography (AR). Ctrl, control (untreated cells). Data, means \pm SEM; HCM: $n \geq 3$ (each experiment: 500 valid primary objects/cells per well, ≥ 5 wells/sample). † $p \geq 0.05$ (not significant), ** $p < 0.01$, ANOVA. See also Figure 4-6.

Figure S4. GABARAPs interact directly with NUFIP2 and G3BP1. (A) Immunoblot analysis of proteins associated with lysosomes purified by anti-HA immunoprecipitation (LysolP; TMEM192-3xHA) from parental HeLa (WT), LC3^{TKO}, GBRP^{TKO} and hexa^{KO} cells treated with 4 mM LLOMe for 30 min. (B) GST pull-down assay of *in vitro* translated and radiolabeled Myc-tagged NUFIP2 deletions with GST or GST-tagged GABARAP(GABA). (C) GST pull-down assay of *in vitro* translated and radiolabeled Myc-tagged NUFIP2 with GST or GST-tagged GABARAP deletions. (D) GST pull-down assay of *in vitro* translated and radiolabeled Myc-tagged NUFIP2/G3BP1 with GST or GST-tagged GABARAP mutants. (E) Immunoblot analysis of denaturing HA immunoprecipitation performed on untreated or 4 mM LLOMe treated (30 min) lysates

from ATG8 knockout (hexa^{KO}) or ATG4/ATG8 knockout (deca^{KO}) HeLa cells expressing HA-GBRPL1-G. (F) GST pull-down assay of *in vitro* translated and radiolabeled Myc-tagged G3BP1 with GST or GST-tagged GABARAP deletions. (G) Summary of interactions between GABARAP and G3BP1. (H) GST pull-down assay of *in vitro* translated and radiolabeled Myc-tagged G3BP1 with GST or GST-tagged NUFIP2. (I) Quantification of Figure S4H. Data (% binding) represents the percentage of the corresponding protein relative to its input. (J) GST pull-down assay of *in vitro* translated and radiolabeled Myc-tagged NUFIP2 with GST or GST-G3BP1. (K) GST pull-down assay of *in vitro* translated and radiolabeled GFP-tagged NUFIP2 with GST or GST-tagged G3BP1 deletions. (L) Immunoblot analysis of interaction between NUFIP2 and G3BP1 in HEK293T cells transfected with FLAG or FLAG-NUFIP2 with 2 mM LLOMe treatment for 30 min. (M) HCM images corresponding to Figure 8C. White masks, algorithm-defined cell boundaries. Yellow masks, computer-identified overlap of mTOR and LAMP2. Ctrl, control (untreated cells). Autoradiography (AR). Data, means \pm SEM; HCM: $n \geq 3$ (each experiment: 500 valid primary objects/cells per well, ≥ 5 wells/sample). ** $p < 0.01$, ANOVA. See also Figure 7 and Figure 8.

Figure S5. Atg8ylation participates in mTOR inactivation in response to lysosomal damage. (A) Quantification by HCM of overlaps between mTOR and LAMP2 in HeLa (WT), GBRP^{TKO} and GBRP^{TKO} transfected with GFP-GABARAP/ GABARAPL1/ GABARAPL. Cells treated with 4 mM LLOMe for 30 min. White masks, algorithm-defined cell boundaries. Yellow masks, computer-identified overlap of mTOR and LAMP2. (B) Quantification by HCM of G3BP1 puncta in HeLa (WT), GBRP^{TKO} and GBRP^{TKO} transfected with GFP-GABARAP/ GABARAPL1/ GABARAPL. Cells were treated with 4 mM LLOMe for 30 min. Red masks, computer-identified G3BP1 puncta. (C) Immunoblot analysis of GABARAP(GABA) lipidation in U2OS cells treated with 2 mM LLOMe for indicated time points. (D) Immunofluorescence confocal microscopy imaging of GFP-GABARAP and LAMP2. U2OS cells overexpressing GFP-GABARAP were treated with 2 mM LLOMe for 30 min and stained for endogenous LAMP2. Scale bar, 5 μ m. (E) WB analysis of ATG9^{KO}, ATG3^{KO} in Huh7 cells. (F) WB analysis of FIP200^{KO}, ATG16L1^{KO} in Huh7 cells. (G) WB analysis of ATG3^{KO}, ATG13^{KO} in HeLa cells. (H) HCM images of Figure 9A. Yellow masks, computer-identified overlap of mTOR and LAMP2. (I) HCM images of Figure 9C. Yellow masks, computer-identified overlap of mTOR and LAMP2. (J) HCM images of Figure 9E, Yellow masks, computer-identified overlap of mTOR and LAMP2. (K) WB analysis of indicated proteins in ATG3^{KO}, ATG16L1^{KO} Huh7 cells. (L) Confocal microscopy imaging (i) and quantification by HCM (ii) of overlaps between mTOR and LAMP2 in parental Huh7 (WT) and ATG3 knockout Huh7 cells (ATG3^{KO}) transfected with scrambled siRNA as control (SCR) or NUFIP2 siRNA (NUFIP2^{KD}). Cells were treated with 2 mM LLOMe for 30 min. WB analysis of indicated protein in (iii). (M) WB analysis of the expression of GFP-SARS-CoV-2^{ORF3a} in HeLa Flp-In^{TetON} GFP-SARS-CoV-2^{ORF3a} cells induced by tetracycline (Tet) for 16 h. (N) Immunoblot analysis of interaction between GCN1 and GFP-ORF3a in HEK293T Flp-In^{TetON} GFP-SARS-CoV-2^{ORF3a} cells induced by 1 μ g/mL tetracycline (Tet) for 16 h. Cell lysates were immunoprecipitated (IP) with anti-GFP antibody and immunoblotted for endogenous GCN1. (O) Immunoblot analysis of interaction between GCN1 and ORF3a in HEK293T cells transfected with GFP or GFP-ORF3a. Cell lysates

were immunoprecipitated (IP) with anti-GFP antibody and immunoblotted for endogenous GCN1. Ctrl, control (untreated cells). Data, means \pm SEM; HCM: $n \geq 3$ (each experiment: 500 valid primary objects/cells per well, ≥ 5 wells/sample). † $p \geq 0.05$ (not significant), ** $p < 0.01$, ANOVA. See also Figure 9 and Figure 10.

Materials and methods

Antibodies and reagents

Antibodies from Cell Signaling Technology were G3BP1(1:1000 for Western blot (WB); 1:200 for immunofluorescence (IF)), TIA1(D1Q3K)(1:1000 for WB; 1:200 for IF), DUSP1(E6T5S)(1:1000 for WB), ERK2 (1:1000 for WB), Phospho-eIF2 α (Ser51)(1:1000 for WB), eIF2 α (1:1000 for WB), Phospho-p70 S6 Kinase (Thr389)(108D2)(1:1000 for WB), p70 S6 Kinase (49D7) (1:1000 for WB), Phospho-GCN2 (Thr899)(E1V9M)(1:1000 for WB), GCN2(1:1000 for WB), mTOR (7C10)(1:1000 for WB; 1:400 for IF), Raptor (24C12)(1:1000 for WB), LAMTOR1 (D11H6)(1:1000 for WB), Phospho-ULK1 (Ser757)(1:1000 for WB), ULK1 (D8H5)(1:1000 for WB), Tuberin/TSC2 (D93F12)(1:1000 for WB), RagA (D8B5)(1:1000 for WB), GABARAPL2 (D1W9T)(1:1000 for WB), Phospho-TFEB (Ser211)(E9S8N)(1:1000 for WB), TFEB (#4240)(1:1000 for WB; 1:200 for IF), ATG13(E1Y9V)(1:1000 for WB), FIP200 (D10D11)(1:1000 for WB), Atg9A (D4O9D)(1:1000 for WB), HA-Tag (C29F4)(1:500 for IF) and normal rabbit IgG. Antibodies from Abcam were GFP (ab290)(1:1000 for WB), GFP(ab38689)(for immunoprecipitation (IP)) and Anti-beta Tubulin (1:1000 for WB). Antibodies from Sigma Aldrich: FLAG M2 (F1804)(for IP and 1:1000 for WB), phospho TFEB (Ser142)(1:1000 for WB), anti-ATG7(1:1000 for WB), anti-ATG3(1:1000 for WB), anti-NUFIP2(#AV51676) (1:1000 for WB), anti-NUFIP2(#HPA067443)(1:100 for IF), anti-Phospho-ERK2 T185/187(1:1000 for WB). Other antibodies used in this study were from the following sources: Galectin-8 (sc-28254)(1:200 for WB) and beta-Actin (C4)(1:1000 for WB), normal mouse IgG from Santa Cruz Biotechnology; LAMP2 (H4B4)(1:500 for IF) from DSHB of University of Iowa; Anti-Multi Ubiquitin (1:500 for IF) and ATG16L1(PM040) (1:400 for IF) from MBL International. Galectin-3 (1:1000 for WB; 1:500 for IF); ALIX (1:200 for IF) from BioLegend. Alexa Fluor 488, 568, 647 (1:500 for IF), G3BP1(1:1000 for WB, 1:200 for IF) and secondary antibodies from ThermoFisher Scientific. DMEM, Opti-MEM Reduced Serum Media and EBSS medias from Life Technologies of ThermoFisher Scientific.

Cells and cell lines

HEK293T, HeLa and U2OS cells were from ATCC. Bone marrow derived macrophages (BMMs) were isolated from femurs of ATG9^{fl/fl} LysM-Cre-negative mice and cultured in DMEM supplemented with mouse macrophage colony stimulating factor (mM-CSF, #5228, CST). TSC2 knockout HeLa cells were from David M. Sabatini (MIT, Cambridge). HEK293T cells stably expressing FLAG-Metap2/FLAG-p14 and constitutively active RagB^{Q99L} were from Roberto Zoncu (UC Berkeley). HeLa mATG8 KO cells are from Michael Lazarou (Monash University). Flp-In cell lines were generated using constructs from Terje Johansen. Huh7 cells are from Rocky Mountain laboratories. Cell lines for LysolP were generated using constructs obtained from

Addgene and the details below. Knockout cell lines were generated by CRISPR/Cas9-mediated knockout system.

Plasmids, siRNAs, and transfection

Plasmids used in this study, such as NUFIP2 cloned into pDONR221 using BP cloning, and expression vectors were made utilizing LR cloning (Gateway, ThermoFisher) in appropriate pDEST vectors for immunoprecipitation assay.

NUFIP2 mutants were generated utilizing the QuikChange site-directed mutagenesis kit (Agilent) and confirmed by sequencing (Genewiz). Plasmid transfections were performed using the ProFection Mammalian Transfection System, FuGENE® HD Transfection Reagent (Promega), or Lipofectamine 2000 Transfection Reagent (ThermoFisher Scientific). siRNAs were delivered into cells using either Lipofectamine RNAiMAX (ThermoFisher Scientific).

Oligonucleotide sequences used in this study: NUFIP2 Gateway-sense (5'GGGGACAAGTTTGTACAAAAAAGCAGGCTTCGAGGAGAAGCCCGGCCAGCCACAGCC3'), NUFIP2 Gateway-anti-sense (5'GGGGACCACTTTGTACAAGAAAGCTGGGTCTTATTGATCTGGACTATCCATGGCTTC3'); NUFIP2 Δ NLS sense (5'GATGGTAGTGGATCTGAGAGCAATAGTGCCAAGGGTTGTGAAAAC3'); GABARAP-G (C-terminal glycine residue exposed mutant) sense (5'GGGGACAAGTTTGTACAAAAAAGCAGGCTTCAAGTTCGTGTACAAAGAAG3'), GABARAP-G (C-terminal glycine residue exposed mutant) anti-sense (5'GGGGACCACTTTGTACAAGAAAGCTGGGTCTCAACCGTAGACACTTTTCG3').

siRNAs were from Horizon Discovery: siGENOME Non-Targeting Control siRNA(D-001210-01-05); siGENOME human NUFIP2 SMARTpool siRNA (L-021280-01-0005); siGENOME human G3BP1 SMARTpool siRNA(L-012099-00-0005); siGENOME human G3BP2 SMARTpool siRNA(L-015329-01-0005); siGENOME human DUSP1 SMARTpool siRNA(L-003484-02-0005); siGENOME human EIF2AK1(HRI) SMARTpool siRNA(M-005007-00-0005); siGENOME human EIF2AK2 (PKR) SMARTpool siRNA(M-003527-00-0005); siGENOME human EIF2AK3 (PERK) SMARTpool siRNA(M-004883-03-0005); siGENOME human EIF2AK4 (GCN2) SMARTpool siRNA(M-005314-02-0005); siGENOME human RNASET2 SMARTpool siRNA(M-009282-01-0005); siGENOME human TIA1 SMARTpool siRNA(L-013042-02-0005).

Generation of NUFIP2 CRISPR mutant cells

NUFIP2 knockout cells (Huh7^{NUFIP2-KO}) were generated by CRISPR/Cas9-mediated knockout system. The lentiviral vector lentiCRISPRv2 carrying both Cas9 enzyme and a gRNA targeting NUFIP2 (gRNA1: AAGTTTGTATGATCGGCCCAA/gRNA2: TAGCCTGAAGCAGACTGTAA) (VectorBuilder) was transfected into HEK293T cells together with the packaging plasmids psPAX2 and pCMV-VSV-G at the ratio of 5:3:2. Two days after transfection, the supernatant containing lentiviruses was collected. Huh7 cells were infected by the mixed lentiviruses containing gRNA1 or gRNA 2. 36 h after infection, the cells were selected with puromycin (1 mg/mL) for one week in order to select NUFIP2 knockout cells. NUFIP2 knockout was confirmed by western blot.

Selection of single clones was performed by dilution in 96-well, which were confirmed by western blots (Figure S3G).

Generating Flp-In^{TetON} GFP-SARS-CoV-2^{ORF3a} cell line

Transfected Hela / HEK293T Flp-In host cells with ORF3a reconstructed plasmid and the pOG44 expression plasmid at ratio of 9:1. 24 h after transfection, washed the cells and added fresh medium to the cells. 48 h after transfection, split the cells into fresh medium around 25 % confluent. Incubated the cells at 37 °C for 2-3 h until they have attached to the culture dish. Then the medium was removed and added with fresh medium containing hygromycin. Fed the cells with selective medium every 3-4 days until single cell clone can be identified. Picked hygromycin-resistant clones and expanded each clone to test. The tested clones incubated in the medium containing 1 or 10 µg/mL tetracycline overnight were determined by western blot for the expressing of ORF3a.

Bead transfection assay

Bead transfections were performed as previously reported (FUJITA, 2013). Transfection reagent-coated beads were prepared by mixing the beads (Polybead® Amino Microspheres 0.20µm; PolySciences, Inc.) with FuGENE HD Transfection Reagent (E2311; Promega), according to the manufacturer's instructions except that bead suspension was used instead of DNA solution. The resulting bead mixture was mixed with growth medium, and further added to cells by replacing the medium at the final concentration of 0.1 µL bead stock/cell. After incubation with the bead mixture overnight at 37 °C in a CO₂ incubator, the cells were washed twice to remove unattached beads, and fixed for the High content microscopy analysis.

Poly(A) RNA Fluorescence in situ hybridization (FISH) analysis

Cells were fixed in 4 % paraformaldehyde for 5 min. Aspirate the paraformaldehyde and add 100 % Cold methanol to each well for 10 min. Remove the methanol and add 70 % ethanol to each well for at least 10 min. Aspirate the ethanol and add 1 M Tris Ph 8.0 to each well for 5 min. Removed the Tris and add hybridization buffer containing the dilution of 5'-labeled Cy3-Oligo-dT(30) stock (GeneLink) for a final concentration of 1 ng/µL. Incubate at 37 °C for at least one hour. After hybridization, wash samples once with 4 x SSC and then 2 x SSC. Incubation with primary antibodies in 2 x SSC + 0.1 % Triton-X-100 for 2 h, wash three times with 2 x SSC and then incubate with secondary antibodies for 1 h at room temperature. Coverslips were mounted using Prolong Gold Antifade Mountant (ThermoFisher Scientific).

Nuclear extraction assay

Nuclear extraction followed manufacturer's instructions (NBP2-29447). Collect cells (2 x 10⁶) and wash twice with cold 1 x PBS. Cell pellets were resuspended in 200 µL 1 x Hypotonic Buffer (20 mM Tris-HCl (pH 7.4); 10 mM NaCl; 3 mM MgCl₂) on ice for 15 min. Add 10 µL detergent (10 % NP40) and vortex for 10 sec at highest setting. Centrifuge the homogenate for 10 min at 3,000 rpm at 4 °C. Transfer and save the supernatant. This supernatant contains the cytoplasmic fraction. The pellet is the nuclear fraction. Resuspend nuclear pellet in 20 µL complete Cell Extraction Buffer (10

mM Tris-HCl (pH 7.4); 100mM NaCl; 1 mM Na₂EDTA; 1 mM EGTA; 10 % Glycerol; 0.5 % Sodium deoxycholate; 1% Triton X-100; 0.1% SDS; 20 mM Sodium pyrophosphate; 2 mM Na₃VO₄; 1 mM NaF; 1 mM PMSF) for 30 min on ice with vortexing at 10 min intervals. Centrifuge for 30 min at 14,000 x g at 4 °C. Transfer supernatant (nuclear fraction) to a clean microcentrifuge tube. Mix with 2 x Laemmli sample buffer (Bio-Rad) and subjected to immunoblot analysis.

LysolP assay

Lentiviruses constructs for generating stable LysolP cells were purchased from Addgene. HEK293T cells were transfected with pLJC5-TMEM192-3xHA or pLJC5-TMEM192-2xFLAG constructs in combination with pCMV-VSV-G and psPAX2 packaging plasmids, 60 h after transfection, the supernatant containing lentiviruses was collected and centrifuged to remove cells and then frozen at -80 °C. To establish LysolP stably expressing cell lines, cells were plated in 10cm dish in DMEM with 10 % FBS and infected with 500 µL of virus-containing media overnight, then add puromycin for selection.

Selected cells in 15 cm plates with 90 % confluency were used for each LysolP. Cells with or without treatment were quickly rinsed twice with PBS and then scraped in 1mL of KPBS (136 mM KCl, 10 mM KH₂PO₄, pH7.25 was adjusted with KOH) and centrifuged at 3000 rpm for 2 min at 4 °C. Pelleted cells were resuspended in 950 µL KPBS and reserved 25 µL for further processing of the whole-cell lysate. The remaining cells were gently homogenized with 20 strokes of a 2 mL homogenizer. The homogenate was then centrifuged at 3000 rpm for 2 min at 4 °C and the supernatant was incubated with 100 µL of KPBS prewashed anti-HA magnetic beads (ThermoFisher) on a gentle rotator shaker for 15 min. Immunoprecipitants were then gently washed three times with KPBS and eluted with 2 x Laemmli sample buffer (Bio-Rad) and subjected to immunoblot analysis.

LysolP proteinase K protection assay

The lysosomes were isolated by LysolP assay and immunopurified by anti-HA magnetic beads (ThermoFisher). The protocols of proteinase K protection assay by Zhang et al, (2015) and Kimura et al (2017) were followed. Briefly, immunoprecipitates were gently washed three times with KPBS and resuspended in 30 µL of B88 (20 mM HEPES-KOH, pH 7.2, 250 mM sorbitol, 150 mM potassium acetate and 5 mM magnesium acetate) or B88 containing 30 µg/mL proteinase K with or without 0.5 % Triton X-100, and stored on ice for 30 min. The reactions were stopped by adding 4 x Laemmli sample buffer (Bio-Rad) and then boiled for 10 min for immunoblot analysis.

LysoTracker Assay

Prepare fresh LysoTracker Staining Solution (2 mL LysoTracker in 1mL medium). Add 10 mL LysoTracker Staining Solution to no treatment, 1 mM LLOMe treated or LLOMe washout cells in 96 wells for total 100 mL per well and incubate at 37°C for 30 min protected from light. Rinse gently by 1X PBS and fix in 4% Paraformaldehyde for 2min. Wash once by 1X PBS and blot with Hoechst 33342 for 2 min before detecting by high content microscopy.

Protein translation assay

Cells in 96 well plates were subjected to indicated treatment and then stained with O-propargyl-puromycin (OPP) using the Click-iT Plus OPP Alexa Fluor 488 protein synthesis assay kit (ThermoFisher) in accordance with the manufacturer's guidelines. Cells were scanned by High content microscopy (HCM), described below. We quantified by HCM the overall fluorescence intensity in cells of fluorescently labeled O-propargyl-puromycin (OPP). OPP is an alkyne analog of puromycin that following incorporation into polypeptides can be fluorescently labeled by Alexa 488 picolyl azide via a chemoselective ligation or 'click' reaction, occurring between the picolyl azide dye and the OPP alkyne.

Murine tuberculosis infection assay

Mycobacterium tuberculosis Erdman culture was prepared by thawing frozen stock aliquot and grown in 7H9 Middlebrook liquid medium supplemented with oleic acid, albumin, dextrose and catalase (OADC, Becton Dickinson, Inc., Sparks, MD, USA), 0.5 % glycerol and 0.05 % Tween 80. Cultures were grown at 37 °C. BMMs were infected with Erdman at indicated MOI and incubated with full medium for 18 h. The infected BMMs were lysed and plated on 7H11 agar plates. CFU was enumerated 3-4 weeks later.

GST pull-down assay

GST and GST-tagged proteins were produced in SoluBL21 Competent *E. coli* (Genlantis, C700200) and purified by binding to Glutathione Sepharose 4 Fast Flow beads (GE Healthcare, 17-5132-01) while myc-tagged proteins were *in vitro* translated using the TNT T7 Reticulocyte Lysate System (Promega, 14610) in the presence of 35S-methionine. 10 mL of translated protein were incubated with immobilized GST-tagged protein in NETN-buffer (50 mM Tris [pH 8.0], 150 mM NaCl, 1 mM EDTA, 0.5 % NP-40) supplemented with cOmplete Mini EDTA-free protease inhibitor cocktail tablets (Roche, 11836170001, 1 tablet/10 mL) for 1 h at 4 °C followed by five times washing with NETN buffer. 2 x SDS gel loading buffer were added and protein separated by SDS-PAGE. Gels were stained with Coomassie Brilliant Blue R-250 Dye (ThermoFisher Scientific, 20278) to visualize the fusion proteins. Radioactive signals were detected by Fujifilm bioimaging analyzer BAS-5000 and quantified with ScienceLab ImageGauge software (Fujifilm).

High content microscopy (HCM)

Cells in 96 well plates were fixed in 4 % paraformaldehyde for 5 min. Cells were then permeabilized with 0.1 % saponin in 3 % Bovine serum albumin (BSA) for 30 min followed by incubation with primary antibodies for 2 h and secondary antibodies for 1 h. Hoechst 33342 staining was performed for 3 min. HCM with automated image acquisition and quantification was carried out using a Cellomics HCS scanner and iDEV software (ThermoFisher Scientific). Automated epifluorescence image collection was performed for a minimum of 500 cells per well. Epifluorescence images were machine analyzed using preset scanning parameters and object mask definitions. Hoechst 33342 staining was used for autofocus and to automatically define cellular outlines based on background staining of the cytoplasm. Primary objects were cells, and regions of

interest (ROI) or targets were algorithm-defined by shape/segmentation, maximum/minimum average intensity, total area and total intensity, etc., to automatically identify puncta or other profiles within valid primary objects. All data collection, processing (object, ROI, and target mask assignments) and analyses were computer driven independently of human operators. HCM also provides a continuous variable statistic since it does not rely on parametric reporting cells as positive or negative for a certain marker above or below a puncta number threshold.

Co-immunoprecipitation (co-IP) and Immunoblotting assays

For co-IP, cells transfected with 8-10 µg of plasmids were lysed in ice-cold NP-40 buffer (ThermoFisher Scientific) supplemented with protease inhibitor cocktail (Roche, 11697498001) and 1 mM PMSF (Sigma, 93482) for 30 min on ice. Lysates were centrifuged for 10 min at 10,000g at 4°C. Supernatants were incubated with (2-3 µg) antibodies overnight at 4 °C. The immune complexes were captured with Dynabeads (ThermoFisher Scientific), followed by three times washing with 1 x PBS. Proteins bound to Dynabeads were eluted with 2 x Laemmli sample buffer (Bio-Rad) and subjected to immunoblot analysis.

For immunoblotting, lysates were centrifuged for 10 min at 10,000g at 4°C. Supernatants were then separated on 4–20% Mini-PROTEAN® TGX™ Precast Protein Gels (Biorad) and transferred to nitrocellulose membranes. Membranes were blocked in 3% BSA for 1 h at RT and incubated overnight at 4°C with primary antibodies diluted in blocking buffer. They were then incubated with an HRP conjugated secondary antibody, and proteins were detected using ECL and developed using ChemiDoc Imaging System (Biorad) or X-ray film. Analysis and quantification of bands was performed using ImageJ software.

Immunofluorescence confocal microscopy and analysis

Cells were plated onto coverslips in 6-well plates. After treatment, cells were fixed in 4 % paraformaldehyde for 5 min followed by permeabilization with 0.1 % saponin in 3 % BSA for 30 min. Cells were then incubated with primary antibodies for 2 h and appropriate secondary antibodies Alexa Fluor 488 or 568 (ThermoFisher Scientific) for 1 h at room temperature. Coverslips were mounted using Prolong Gold Antifade Mountant (ThermoFisher Scientific). Images were acquired using a confocal microscope (META; Carl Zeiss) equipped with a 63 3/1.4 NA oil objective, camera (LSM META; Carl Zeiss), and AIM software (Carl Zeiss).

Time-Lapse Imaging of Cultured Cells

U2OS cell expressing mCherry-G3BP1 and GFP-LAMP1, were incubated with 2 mM LLome for live-cell fluorescence image which was performed using an inverted microscope (confocal TCS SP5, Leica, LAS AF version 2.6.0), a 63 x PlanAPO oil-immersion objective lens (NA 1.4). Two-color time-lapse images were acquired at 340 ms intervals and z-stacks collapsed into 2D projections to generate movies.

RNA-sequencing

HEK293T cells were treated with 1 mM LLOMe or 2 mM LOME for 30 min. Total RNA was extracted using RNeasy Kits (QIAGEN) following the manufacturer's protocol. The RNA-sequencing service was performed by LC Sciences (Houston, Texas). Total RNA quantity and purity were analyzed using a Bioanalyzer 2100 and a RNA 6000 Nano LabChip kit (Agilent), with RNA integrity values of >7.0. Poly(A) RNA was purified from total RNA (5 µg) using poly-T oligo-attached magnetic beads using two rounds of purification. Following purification, the mRNA was fragmented into small pieces using divalent cations under elevated temperature. Then the cleaved RNA fragments were reverse-transcribed to create the final cDNA library in accordance with the protocol for the TruSeq RNA Sample Preparation v.2 (cat. no. RS-122-2001, RS-122-2002) (Illumina); the average insert size for the paired-end libraries was 300 bp (±50 bp). The paired-end sequencing was carried out on an Illumina Novaseq™ 6000 at LC Sciences following the manufacturer's recommended protocol. Using the Illumina paired-end RNA-seq approach, the transcriptome was sequenced, generating a total of 2 x 150 million bp paired-end reads. This yielded gigabases (Gb) of sequence. Before assembly, the low-quality reads (defined as (1) reads containing sequencing adaptors, (2) reads containing sequencing primer; and (3) nucleotide with a q quality score lower than 20) were removed. Sequencing reads were aligned to the reference genome using HISAT2 package. HISAT allows multiple alignments per read (up to 20 by default) and a maximum of two mismatches when mapping the reads to the reference. HISAT builds a database of potential splice junctions and confirms these by comparing the previously unmapped reads against the database of putative junctions. The mapped reads of each sample were assembled using StringTie. All transcriptomes from samples were merged to reconstruct a comprehensive transcriptome using perl scripts (LC Sciences). After the final transcriptome was generated, StringTie and edgeR were used to estimate the expression levels of all transcripts. StringTie was used to calculate the expression level for mRNAs via the FPKM (fragments per kilobase million) values. Differential gene expression was analysed using the R package edgeR, which considers dispersions (that is, variations) between biological replicates. P values were calculated using Fisher's exact test adapted for overdispersed data; edgeR models read counts with negative binomial (NB) distribution⁶⁴. The differentially expressed mRNAs and genes were selected by R package with log₂(fold change) values of ≥1 or log₂(fold change) values of ≤ -1 and with statistical significance of P < 0.05.

LysoIP-LC/MS/MS DIA

LysoIP-LC/MS/MS DIA were performed at UC Davis Proteomics Core Facility (Davis, CA). Protein samples on magnetic beads were washed four times with 200 µL of 50 mM Triethyl ammonium bicarbonate (TEAB) with a 20 min shake time at 4 °C in between each wash. Roughly 2.5 mg of trypsin was added to the bead and TEAB mixture and the samples were digested over night at 800 rpm shake speed. After overnight digestion the supernatant was removed, and the beads were washed once with enough 50 mM ammonium bicarbonate to cover. After 20 min at a gentle shake the wash is removed and combined with the initial supernatant. The peptide extracts are reduced in volume by vacuum centrifugation and a small portion of the extract is used for fluorometric peptide quantification (Thermo scientific Pierce). One microgram of sample based on the fluorometric peptide assay was loaded for each LC/MS analysis.

Peptides were separated on an Easy-spray 100 mm x 25 cm C18 column using a Dionex Ultimate 3000 nUPLC. Solvent A=0.1 % formic acid, Solvent B=100 % Acetonitrile 0.1 % formic acid. Gradient conditions = 2 % B to 50 % B over 60 minutes, followed by a 50 %-99 % B in 6 min and then held for 3 min than 99 % B to 2 % B in 2 min. Total Run time = 90 min. Thermo Scientific Fusion Lumos mass spectrometer running in Data independent Analysis mode. Two gas phases fractionated (GFP) injections were made per sample using sequential 4 Da isolation windows. GFP1 = m/z 362-758, GFP 2 = m/z 758-1158. Tandem mass spectra were acquired using a collision energy of 30, resolution of 30K, maximum inject time of 54 ms and a AGC target of 50K.

DIA Quantification and Statistical Analysis

DIA data was analyzed using Scaffold DIA (1.3.1). Raw data files were converted to mzML format using ProteoWizard (3.0.11748). Analytic samples were aligned based on retention times and individually searched against Pan human library <http://www.swathatlas.org/> with a peptide mass tolerance of 10.0 ppm and a fragment mass tolerance of 10.0 ppm. Variable modifications considered were: Modification on M M and Modification on C C. The digestion enzyme was assumed to be Trypsin with a maximum of 1 missed cleavage site(s) allowed. Only peptides with charges in the range <2..3> and length in the range <6..30> were considered. Peptides identified in each sample were filtered by Percolator (3.01.nightly-13-655e4c7-dirty) to achieve a maximum FDR of 0.01. Individual search results were combined and peptide identifications were assigned posterior error probabilities and filtered to an FDR threshold of 0.01 by Percolator (3.01.nightly-13-655e4c7-dirty). Peptide quantification was performed by Encyclopedia (0.8.1). For each peptide, the 5 highest quality fragment ions were selected for quantitation. Proteins that contained similar peptides and could not be differentiated based on MS/MS analysis were grouped to satisfy the principles of parsimony. Proteins with a minimum of 2 identified peptides were thresholded to achieve a protein FDR threshold of 1.0%. Raw data and ScaffoldDIA results are available from the MassIVE proteomics repository MassIVE = MSV000088152 and Proteome Exchange = PXD028745. Reviewer password for Proteome Exchange = Atg8ylation.

Quantification and statistical analysis

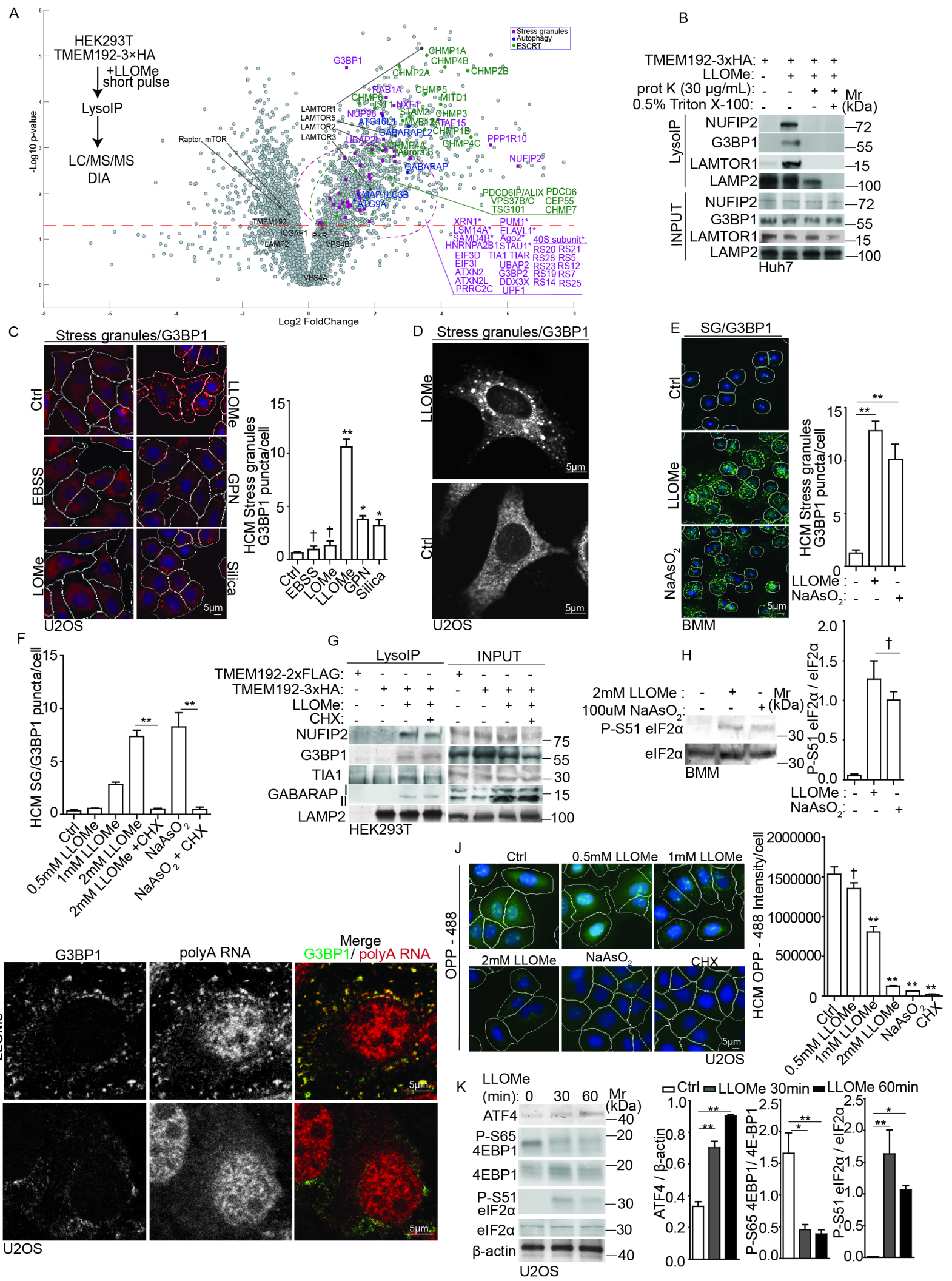
Data in this study are presented as means \pm SEM ($n \geq 3$). Data were analyzed with either analysis of variance (ANOVA) with Tukey's HSD post-hoc test, or a two-tailed Student's t test. For HCM, $n \geq 3$ includes in each independent experiment: 500 valid primary objects/cells per well, from ≥ 5 wells per plate per sample. Statistical significance was defined as: † (not significant) $p \geq 0.05$ and * $p < 0.05$, ** $p < 0.01$.

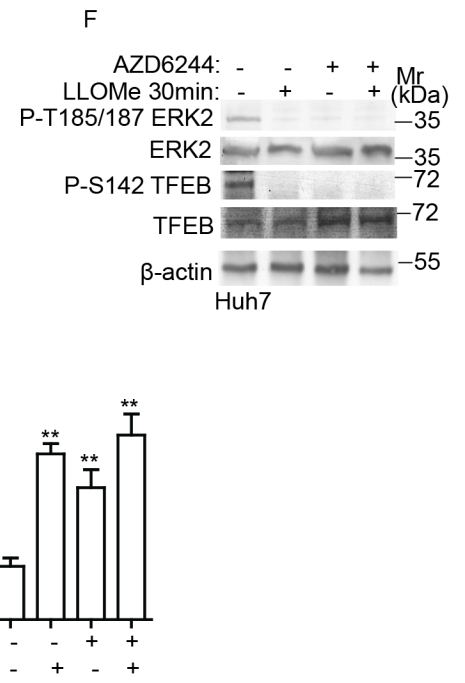
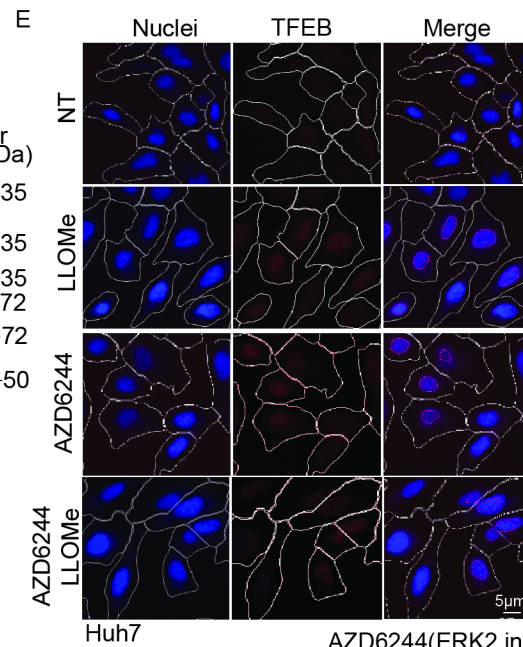
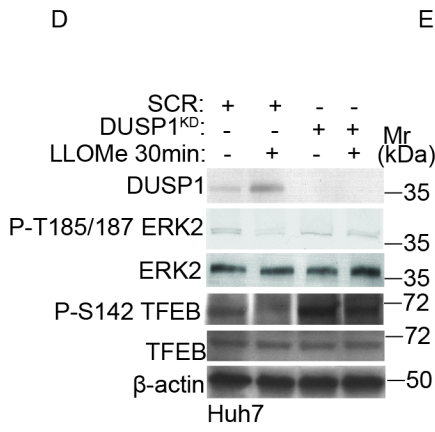
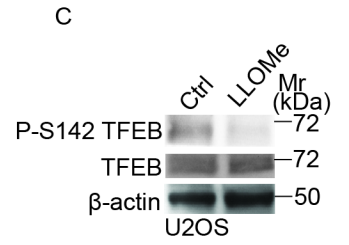
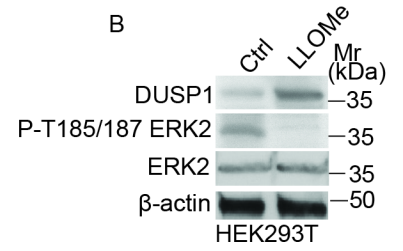
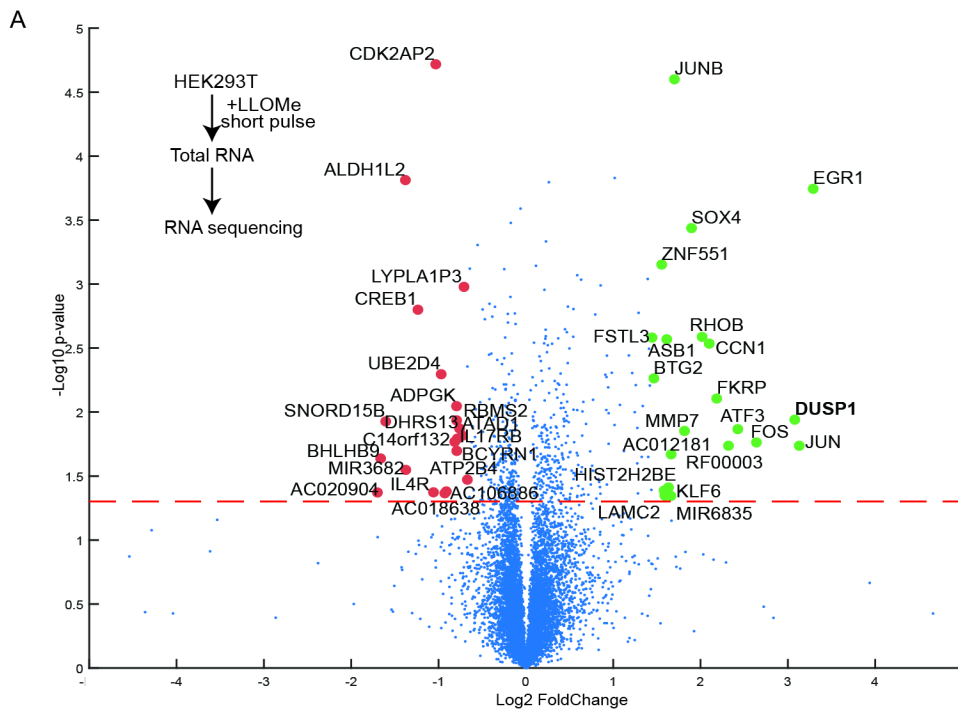
Data and code availability

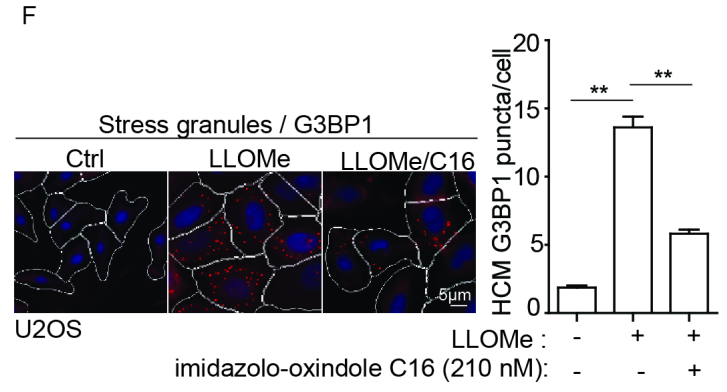
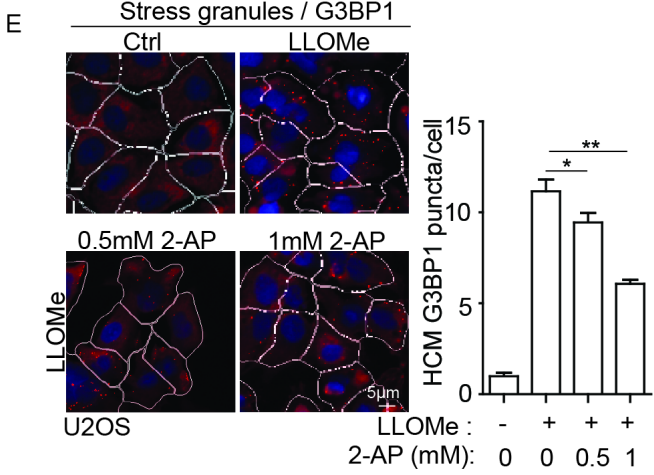
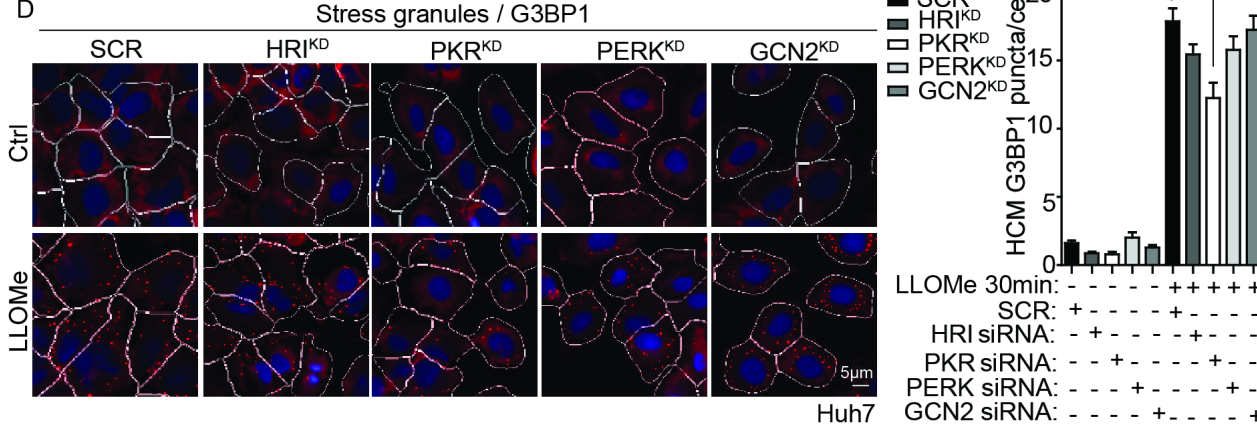
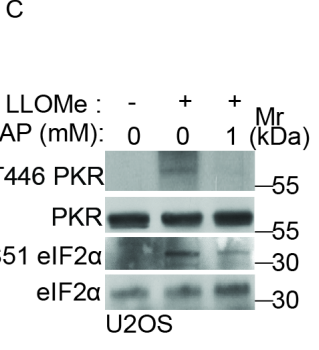
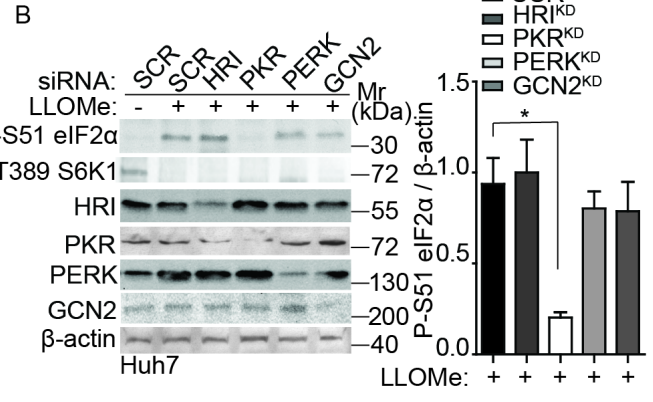
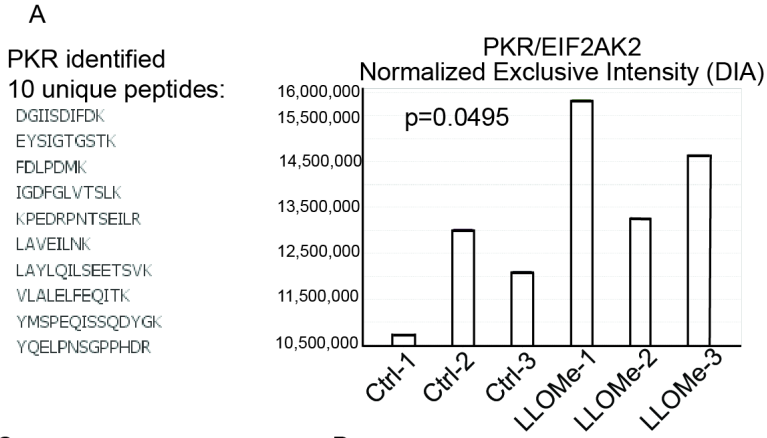
Raw MS DIA data of LysolP in HEK293T cells have been deposited at the MassIVE proteomics repository MassIVE = MSV000088152 and Proteome Exchange = PXD028745. Reviewer password for Proteome Exchange = Atg8ylation. The rest of raw MS DIA/DDA data in this study have been deposited at the MassIVE proteomics repository MassIVE = MSV000089622 and Proteome Exchange = PXD034414. Reviewer password for Proteome Exchange = mTOR.

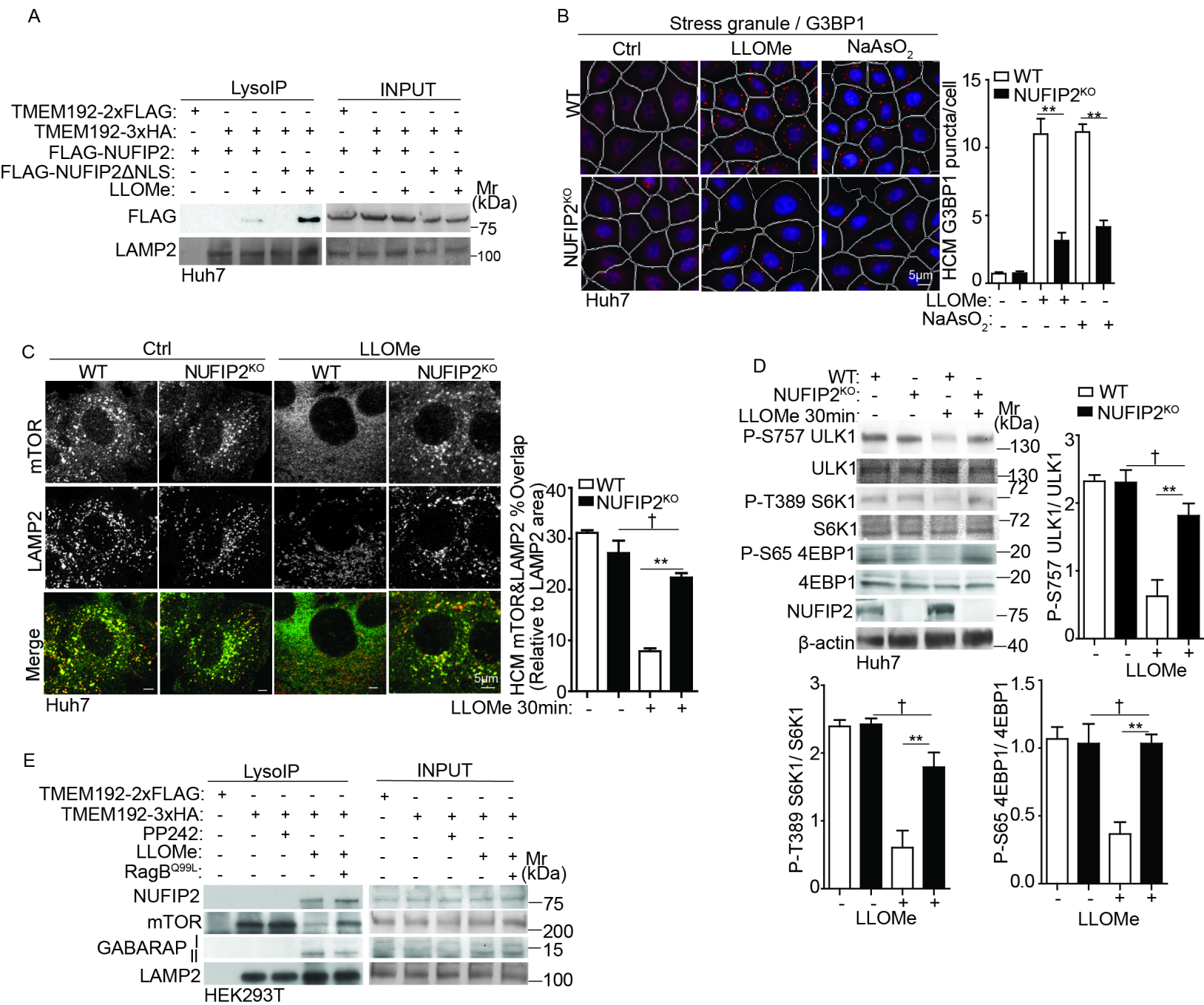
Online supplemental material

[Fig. S1](#) shows stress granule formation during lysosomal damage. [Fig. S2](#) shows the dynamic interactions between stress granules and lysosomes during lysosomal damage. [Fig. S3](#) shows NUFIP2 exits nucleus and localizes to lysosomes upon damage and cooperates with galectin-8 in mTORC1 response to lysosomal damage. [Fig. S4](#) shows GABARAPs interact directly with NUFIP2 and G3BP1. [Fig. S5](#) shows atg8ylation participates in mTOR inactivation in response to lysosomal damage. [Table S1](#) includes all the raw MS DIA data of this study and corresponding analysis. [Movie 1](#) shows dynamic interactions between stress granules and lysosomes during lysosomal damage. [Movie 2-4](#) show the enlarged region of interest in [Movie 1](#).





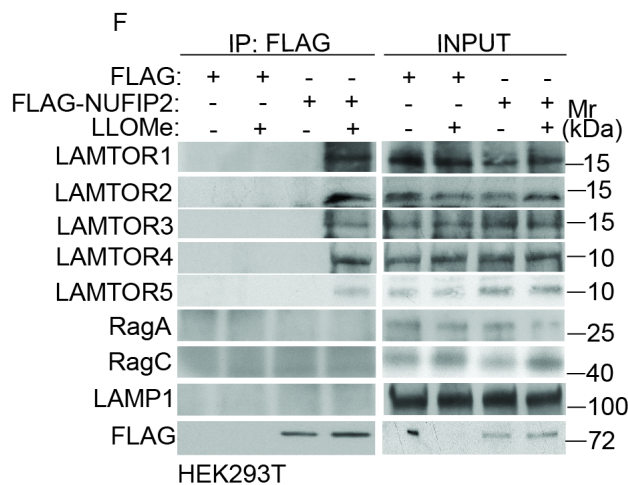
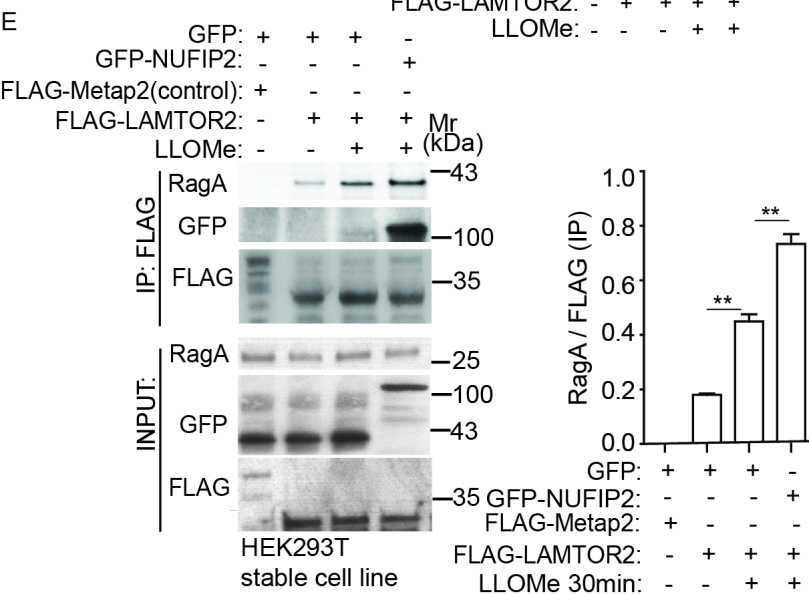
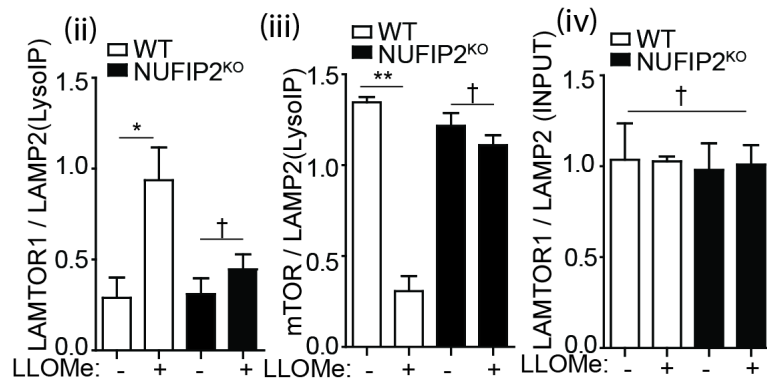
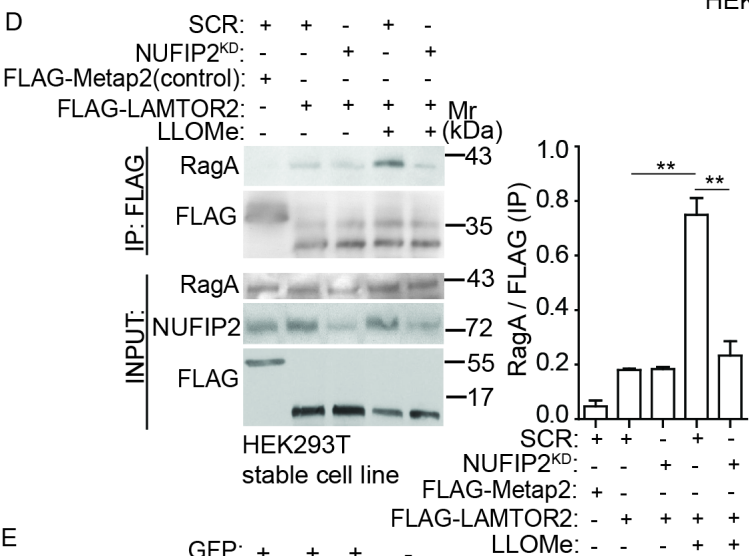
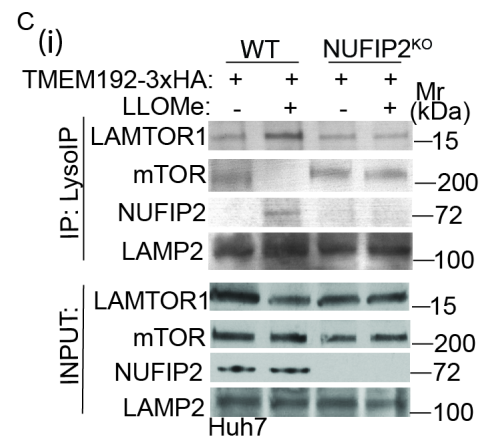
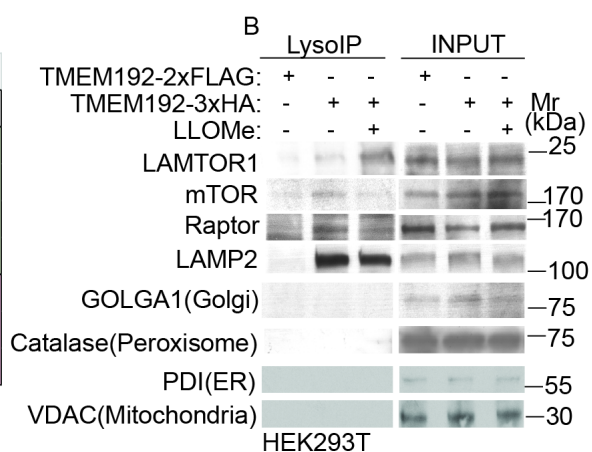


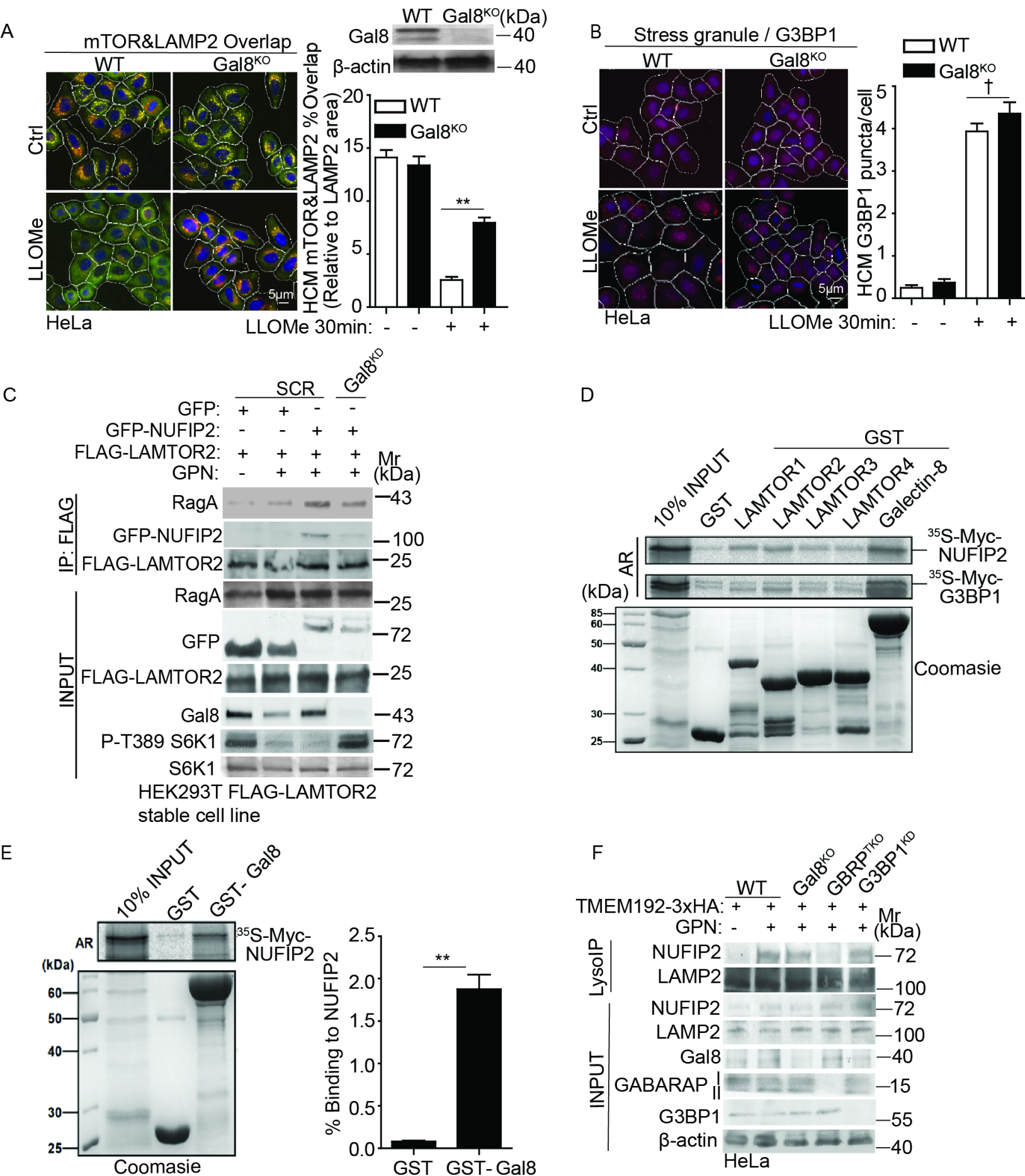


A

| Protein | p-value | Log2 FC |
|---------|-------------|----------|
| LAMTOR1 | 6.76E-06 | 3.41428 |
| LAMTOR2 | 0.001125442 | 2.343996 |
| LAMTOR3 | 0.007919951 | 1.981497 |
| LAMTOR5 | 7.50E-04 | 2.732261 |
| mTOR | 0.030536 | -0.5615 |
| Raptor | 0.012898699 | -0.78684 |
| mLST8 | 0.002914537 | -1.05052 |

HEK293T





A

| LysolP-MS: Significantly increased autophagy factors | | | |
|---|---------|---------|----------|
| Protein | p-value | Log2 FC | Peptides |
| GABARAPL2 | 0.00059 | 2.52 | 7 |
| GABARAP | 0.0019 | 2.39 | 3 |
| MAP1LC3B | 0.01109 | 1.4515 | 2 |
| ATG9A | 0.00082 | 1.71 | 10 |
| ATG16L1 | 0.0002 | 2.23 | 7 |

